# Multi-wavelength study of a young open cluster NGC 7419

Himali Joshi[1], Brijesh Kumar[1,2], K. P. Singh[3], Ram Sagar[1], Saurabh Sharma[1], J. C. Pandey[1]

[1] *Aryabhatta Research Institute of Observational Sciences, Manora Peak, Nainital 263 129, India*
[2] *Departamento de Física, Universidad de Concepción, Casilla 160-C, Concepción, Chile*
[3] *Tata Institute of Fundamental Research, Mumbai 400 005, India*

10 September 2008

**ABSTRACT**

Using new *UBVRI* Hα CCD photometric observations and the archival infrared and X-ray data, we have carried out a multi-wavelength study of a Perseus arm young galactic star cluster NGC 7419. An age of $22.5 \pm 3.0$ Myr and a distance of $3230^{+330}_{-430}$ pc are derived for the cluster. Our photometric data indicates a higher value of color excess ratio $E(U-B)/E(B-V)$ than the normal one. There is an evidence for mass segregation in this dynamically relaxed cluster and in the range $1.4 - 8.6 M_\odot$, the mass function slope is in agreement with the Salpeter value. Excess emissions in near-infrared and Hα support the existence of a young ($\leq 2$ Myr) stellar population of Herbig Ae/Be stars ($\geq 3.0 M_\odot$) indicating a second episode of star formation in the cluster region. Using XMM-Newton observations, we found several X-ray sources in the cluster region but none of the Herbig Ae/Be stars is detected in X-rays. We compare the distribution of upper limits for Herbig Ae/Be stars with the X-ray distribution functions of the T-Tauri and the Herbig Ae/Be stars from previous studies, and found that the X-ray emission level of these Herbig Ae/Be stars is not more than $L_X \sim 5.2 \times 10^{30}$ erg s$^{-1}$, which is not significantly higher than for the T-Tauri stars. Therefore, X-ray emission from Herbig Ae/Be stars could be the result of either unresolved companion stars or a process similar to T-Tauri stars. We report an extended X-ray emission from the cluster region NGC 7419, with a total X-ray luminosity estimate of $\sim 1.8 \times 10^{31}$ erg s$^{-1}$ arcmin$^{-2}$. If the extended emission is due to unresolved emission from the point sources then we estimate $\sim$288 T-Tauri stars in the cluster region each having X-ray luminosity $\sim 1.0 \times 10^{30}$ erg s$^{-1}$. Investigation of dust attenuation and $^{12}$CO emission map of a square degree region around the cluster indicates the presence of a foreground dust cloud which is most likely associated with the local arm star forming region (Sh2-154). This cloud harbors uniformly distributed pre-main-sequence stars ($0.1 - 2.0 M_\odot$), with no obvious trend of their distribution with either $(H-K)$ excess or $A_V$. This suggests that the star formation in this cloud depend mostly upon the primordial fragmentation.

**Key words:** star clusters : young – star formation : primordial fragmentation – young stellar objects : Herbig Ae/Be, T Tauri, X-ray emission

## 1 INTRODUCTION

NGC 7419 (RA$_{J2000}$ = 22$^h$54$^m$20$^s$, DEC$_{J2000}$ = +60°48′54″; $l = 109°.13$, $b = 1°.12$), is a moderately populated young and heavily reddened galactic star cluster in Cepheus with a large number of Be stars. The cluster contains high mass ($\geq 10 M_\odot$); intermediate mass ($2 - 10 M_\odot$) and low-mass ($\leq 2 M_\odot$) stars. It is therefore an ideal laboratory for the study of initial stellar mass distribution as well as duration of star formation process in a molecular cloud. Presence of

statistically significant number of Herbig Ae/Be stars in the cluster makes it very attractive for understanding the formation of these stars and origin of various atmospheric activities like Hα emission and X-ray emission in them. However, to address these questions in detail, one would like to know accurate distance and age parameters of the cluster NGC 7419, which is lacking despite a number of photometric and spectroscopic studies. This is mainly because of the fact that the cluster is heavily reddened in comparison to the nearby

clusters situated at the similar distances, and suffers from variable reddening.

In order to determine cluster reddening reliably, accurate $UBV$ broadband photometry of early type stars is essential. A comparison of the photometries available in the literature indicates that $UB$ data, many have systematic calibration error. For example, Beauchamp, Moffat & Drissen (1994) have mentioned that their color may have an offset of $\sim 0.2$ mag due to the calibration problems in $U$ band. Their photometric observations have been carried out in the poor seeing ($2''.5 - 4''.0$) conditions. This will affect cluster photometric data particularly in the crowded regions.

The main goals of present study are to determine the distance, age and its spread, and mass function (MF) of the cluster as accurate as possible. This will help us to understand the star formation history of the cluster, and to investigate the X-ray emission properties of Herbig Ae/Be stars. Deep optical $UBVRI$ observations ($V \sim 22.0$ mag), narrow band H$\alpha$ photometric observations along with the Two Micron All Sky Survey (2MASS), Infrared All Sky Survey (IRAS), Midcourse Space experiment (MSX) and XMM-Newton archival data are used to understand the X-ray emission properties of Herbig Ae/Be stars, and the global scenario of star formation in the cluster NGC 7419 and its surrounding region.

Blanco et al. (1955) has reported the distance of this cluster as $\sim 6$ kpc based on the $RI$ photometric observations. A similar value for cluster distance has also been obtained by Moffat & Vogt (1973). However, van de Hulst et al. (1954) has obtained a significantly smaller distance of 3.3 kpc. Using CCD data, a distance of 2.0 kpc and 2.3 kpc was estimated by Bhatt et al. (1993) and Beauchamp, Moffat & Drissen (1994), respectively. The age estimated by Bhatt et al. (1993) is $\sim 40$ Myr while Beauchamp, Moffat & Drissen (1994) have estimated a much younger age of $\sim 14$ Myr. Recent CCD observations reported by Subramaniam et al. (2006) estimated its distance as 2.9 kpc and an age of 20–25 Myr.

The paper describes optical observations and the derivation of cluster parameters in §2 and §3. The near-infrared (NIR) data are dealt in §4, while distribution of young stellar objects (YSOs), MF and mass segregation are given in §5, §6 and §7. Finally, the X-ray data and its analysis (for the first time) are described in §8, followed by the summary and conclusions in §9.

## 2 PHOTOMETRIC DATA

### 2.1 Observations

The optical observations of NGC 7419 were carried out using a thinned back-illuminated CCD camera mounted at f/13 Cassegrain focus of the 104-cm Sampurnanand reflector telescope of Aryabhatta Research Institute of Observational Sciences, Nainital. A $24\mu$m square pixel of the $2048 \times 2048$ size CCD detector corresponds to $0''.38$ and the entire chip covers a field of about $13' \times 13'$ on the sky. In order to improve the signal to noise ratio, observations were taken in binned mode of $2 \times 2$ pixel. The gain and readout noise of the CCD are 10 electron per analog-to-digital unit and 5.3 electron, respectively. The journal of optical observations is given

**Table 1.** Journal of CCD observations of the cluster NGC 7419 and the calibration region SA98 (Landolt 1992).

| Date(UT) | Filter | Exposure Time (s) ($\times$no. of exposures) |
|---|---|---|
| NGC 7419 | | |
| 30 October 2005 | H$\alpha$ | 300$\times$2, 120$\times$2, 1500$\times$3 |
| | H$\alpha$ -cont | 300$\times$2, 120$\times$2, 900$\times$3 |
| 07 November 2005 | $U$ | 300$\times$3, 360$\times$4 |
| | $B$ | 180$\times$4, 240$\times$4 |
| | $V$ | 180$\times$4, 180$\times$4 |
| | $R$ | 20$\times$4, 120$\times$4 |
| | $I$ | 20$\times$4, 60$\times$4 |
| 08 November 2005 | $U$ | 1800$\times$1 |
| | $B$ | 1200$\times$1 |
| | $V$ | 900$\times$1 |
| | $R$ | 300$\times$1 |
| | $I$ | 500$\times$1 |
| 25 October 2006 | $U$ | 300$\times$3 |
| | $B$ | 300$\times$2 |
| | $V$ | 100$\times$2 |
| | $R$ | 20$\times$2 |
| | $I$ | 20$\times$2 |
| SA 98 | | |
| 25 October 2006 | $U$ | 360$\times$11 |
| | $B$ | 150$\times$10 |
| | $V$ | 60$\times$10 |
| | $R$ | 25$\times$10 |
| | $I$ | 25$\times$10 |

in Table 1. Broad band Johnson $UBV$, Cousins $RI$ and, narrow band H$\alpha$ line ($\lambda = 656.5$ nm) and H$\alpha$ continuum ($\lambda = 665$ nm) filters were used for observations. The narrow band filters had a full width at half maximum of 8 nm. Several bias and twilight flat field frames in all the filters were taken to clean the images. Multiple long and short exposures were obtained for the cluster region. We observed 12 stars in Landolt (1992) standards field (SA98) covering a range in brightness ($11.93 < V < 15.90$) as well as in color ($0.157 < (B - V) < 2.192$) for calibrating the cluster observations. The airmass range is covered from 1.1 to 2.0 for the Landolt (1992) standards, which was used for extinction determinations.
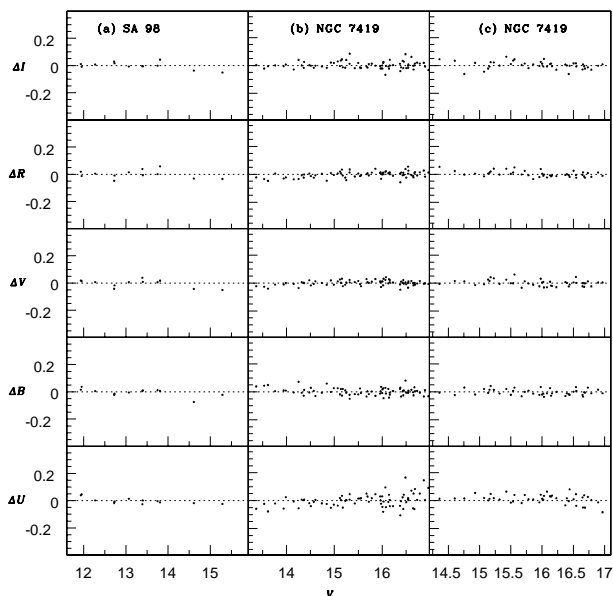
The photometric CCD data were reduced using the IRAF[1] and ESO MIDAS[2] data reduction packages. Photometry of the bias-subtracted and flat-fielded CCD frames was carried out using DAOPHOT-II software (Stetson 1987, 1992). Magnitude of the stars obtained from different frames were averaged separately for short and long exposures. When brighter stars were saturated on deep exposure frames, their magnitudes were taken only from unsaturated short exposure frames. We used DAOGROW program for

**Table 2.** The mean photometric errors ($\sigma$) in magnitude are given as a function of brightness range in the cluster region.

| Magnitude range | $\sigma_U$ | $\sigma_B$ | $\sigma_V$ | $\sigma_R$ | $\sigma_I$ |
|---|---|---|---|---|---|
| < 14 | 0.009 | 0.002 | 0.003 | 0.005 | 0.007 |
| 14 − 15 | 0.007 | 0.005 | 0.003 | 0.005 | 0.004 |
| 15 − 16 | 0.021 | 0.010 | 0.013 | 0.012 | 0.025 |
| 16 − 17 | 0.030 | 0.015 | 0.010 | 0.011 | 0.023 |
| 17 − 18 | 0.069 | 0.018 | 0.010 | 0.012 | 0.026 |
| 18 − 19 | 0.131 | 0.029 | 0.014 | 0.011 | 0.031 |
| 19 − 20 | | 0.070 | 0.017 | 0.013 | 0.026 |
| 20 − 21 | | 0.173 | 0.031 | 0.019 | 0.031 |
| 21 − 22 | | | 0.082 | 0.036 | 0.034 |
| 22 − 23 | | | 0.196 | 0.061 | 0.047 |



**Figure 1.** Difference in *UBVRI* magnitude measurements as a function of $V$ magnitude are shown. The left panels (a) show the residuals of standard magnitude from Landolt (1992) and the present transformed magnitudes, while the middle (b) and right (c) panels show magnitude difference of secondary standards as generated on 25 October 2006 to that of on 07 November 2005 and 08 November 2005, respectively.

construction of an aperture growth curve required for determining the difference between aperture and profile fitting magnitudes.

## 2.2 Calibrations

The instrumental magnitudes were converted into the standard system using least square linear regression procedure outlined by Stetson (1992). The photometric calibration equations used are:

$u = U + (0.588 \pm 0.015)X + (-0.002 \pm 0.004)(U - B) + (6.933 \pm 0.006)$
$b = B + (0.347 \pm 0.013)X + (-0.035 \pm 0.005)(B - V) + (4.771 \pm 0.007)$
$v = V + (0.159 \pm 0.012)X + (-0.041 \pm 0.004)(V - I) + (4.320 \pm 0.007)$
$r = R + (0.139 \pm 0.009)X + (-0.056 \pm 0.007)(V - R) + (4.234 \pm 0.006)$
$i = I + (0.104 \pm 0.007)X + (-0.048 \pm 0.003)(V - I) + (4.767 \pm 0.005)$

where $U, B, V, R$ and $I$ are the standard magnitudes; $u, b, v, r$ and $i$ are the instrumental magnitudes obtained after time and aperture correction; and $X$ is the airmass. We have ignored the second-order color correction terms as they are generally small in comparison to the internal photometric errors as given by DAOPHOT. The photometric errors as a function of brightness range are given in Table 2. It can be seen that the errors become large ($\geq$ 0.1mag) for stars fainter than $V \approx 22$ mag, and hence the measurements beyond this magnitude are less reliable and are not considered in further analysis. At $V$ band, we could detect 1817 stars in $13' \times 13'$ region and their photometric magnitudes are given in Table 3 (available only in electronic form). The difference of calibrated magnitudes derived using above transformation to that of the Landolt (1992) magnitudes are plotted in Figure 1. We generated secondary standards in the cluster field using data of 25th October 2006 to standardise the data observed on 7th and 8th of November 2005. We, therefore also plot differences in magnitudes of the secondary standards on these dates. No systematic effect has been seen in the residuals from night-to-night and its distribution is random in nature with a typical accuracy of $\sim$ 0.03 mag in *UBVRI* band.

Figure 2 shows a comparison of the present CCD photometry with the previously reported CCD photometry by Bhatt et al. (1993), Beauchamp, Moffat & Drissen (1994) and Subramaniam et al. (2006). The difference $\Delta$ (present-literature) is plotted as a function of $V$ magnitude and a detailed statistics are given in Table 4 (available only in electronic form). In comparison to the photometric data of Beauchamp, Moffat & Drissen (1994), the $(B - V)$ colors obtained by us are bluer by $\sim$ 0.25 mag, $(U - B)$ colors are redder by $\sim$ 0.25 mag and the $V$ magnitude is fainter by $\sim$ 0.05 mag. Our photometry is in agreement with Subramaniam et al. (2006) and Bhatt et al. (1993). It is worth pointing out that our data is $\sim$ 2.0 mag deeper from Subramaniam et al. (2006) and Bhatt et al. (1993), i.e., $V \sim$ 22.0 mag.

## 2.3 Completeness of the data

The completeness of the data used in the present work was estimated using the ADDSTAR routine of the DAOPHOT II. In brief, the method consists of randomly adding artificial stars (about 10–15% of the originally detected stars) of known magnitudes and positions into the original frames. The frames were re-reduced using the same procedure used for the original frames. The ratio of the number of recovered stars to those added in each magnitude interval gives the completeness factor (CF) as a function of magnitude. The CF was obtained using the stars which were recovered in both $V$ and $I$ pass-bands. The detailed procedures have been outlined elsewhere (Sagar & Richtler 1991; Sagar & Griffiths 1998; Pandey et al. 2001; Nilakshi & Sagar 2002). The CF as a function of $V$ magnitude is given in Table 5.
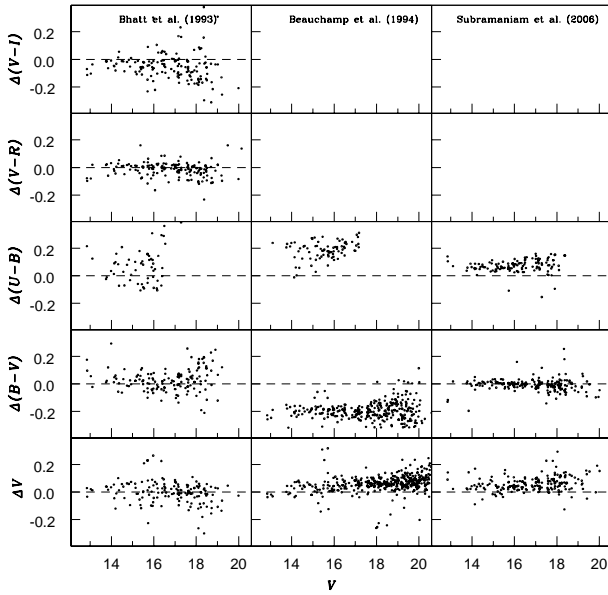
## 2.4 H$\alpha$ photometric data

To identify emission line stars, we use $\alpha$-index ($m_{6565} - m_{6650}$) parameter, where $m_{6565}$ and $m_{6650}$ are the magni-

**Table 3.** $UBVRI$ and H$\alpha$ photometric data of the sample stars in $13' \times 13'$ region. X and Y positions of stars in the CCD are converted into RA$_{J2000}$ and DEC$_{J2000}$ using the Guide Star Catalogue II (GSC 2.2, 2001). The complete table is available in electronic form only.
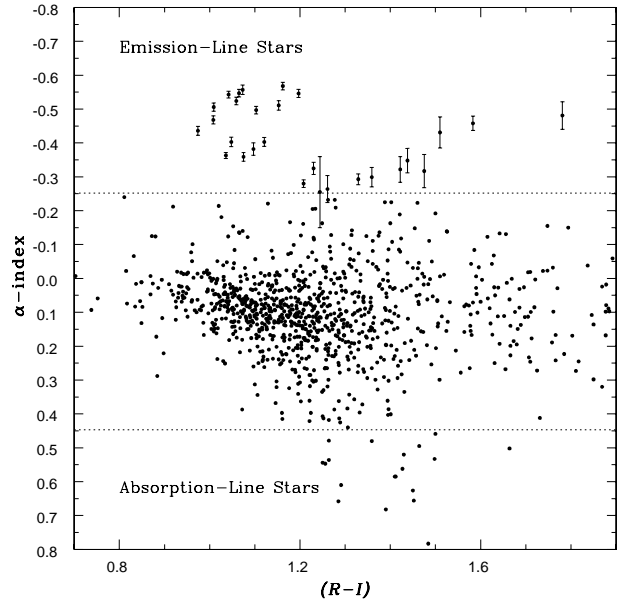
| ID | RA$_{J2000}$ (h m s) | DEC$_{J2000}$ (° ′ ″) | X (pixel) | Y (pixel) | $U$ (mag) | $B$ (mag) | $V$ (mag) | $R$ (mag) | $I$ (mag) | H$\alpha$ -index (mag) |
|---|---|---|---|---|---|---|---|---|---|---|
| 1 | 22 54 06.38 | +60 52 13.30 | 818.710 | 640.714 | $12.999 \pm 0.002$ | $12.481 \pm 0.002$ | $11.707 \pm 0.009$ | $11.321 \pm 0.012$ | $11.003 \pm 0.002$ | $0.032 \pm 0.008$ |
| 2 | 22 54 02.22 | +60 54 57.20 | 1032.410 | 691.088 | $13.518 \pm 0.002$ | $12.964 \pm 0.002$ | $12.156 \pm 0.009$ | $11.761 \pm 0.011$ | $11.381 \pm 0.004$ | $0.038 \pm 0.006$ |
| 3 | 22 53 30.17 | +60 53 38.60 | 914.148 | 994.003 | $13.964 \pm 0.003$ | $13.492 \pm 0.002$ | $12.740 \pm 0.002$ | $12.321 \pm 0.010$ | $11.946 \pm 0.004$ | $0.022 \pm 0.020$ |
| – | – | – | – | – | – | – | – | – | – | – |

**Table 4.** A comparison of present $UBVRI$ CCD photometry with that present in the literature – viz Bhatt et al. (1993), Beauchamp, Moffat & Drissen (1994) and Subramaniam et al. (2006). The complete table is available in electronic form only.

| V range | $< \Delta V >$ $Mean \pm \sigma$ | $< \Delta(B-V) >$ $Mean \pm \sigma$ | $< \Delta(U-B) >$ $Mean \pm \sigma$ | $< \Delta(V-R) >$ $Mean \pm \sigma$ | $< \Delta(V-I) >$ $Mean \pm \sigma$ |
|---|---|---|---|---|---|
| Bhatt et al. (1993) | | | | | |
| < 14.0 | $0.025 \pm 0.030$ (8) | $0.060 \pm 0.070$ (6) | $0.030 \pm 0.083$ (4) | $-0.022 \pm 0.065$ (7) | $-0.044 \pm 0.034$ (6) |
| – | – | – | – | – | – |



**Figure 2.** Comparison of present CCD photometry with that available in the literature. The difference $\Delta$ (present-literature) is in magnitude. The dashed line drawn in each panel represents zero difference.



**Figure 3.** The $\alpha$-index as a function of color $(R-I)$. The dashed line represents the $3\sigma$ limits from a mean $\alpha$-index of $0.096 \pm 0.116$ mag. Emission-line stars having $\alpha$-index $\leq -0.252$ mag are shown with error bars. The absorption line stars denote $\alpha$-index $\geq 0.444$ mag.

**Table 5.** Completeness Factor of the photometric data as a function of brightness and location.

| Magnitude range (V mag) | NGC 7419 $r \leq 1'$ | $1' \leq r \leq 3.5'$ | Field region $3.5' \leq r \leq 5'$ |
|---|---|---|---|
| 13-14 | 1.00 | 1.00 | 1.00 |
| 14-15 | 1.00 | 1.00 | 1.00 |
| 15-16 | 1.00 | 1.00 | 1.00 |
| 16-17 | 1.00 | 0.98 | 0.99 |
| 17-18 | 0.89 | 0.97 | 0.98 |
| 18-19 | 0.57 | 0.93 | 0.96 |
| 19-20 | 0.59 | 0.89 | 0.97 |
| 20-21 | 0.60 | 0.86 | 0.93 |
| 21-22 | 0.15 | 0.38 | 0.47 |

tude of a star in the H$\alpha$ and H$\alpha$ -continuum filter, respectively. In an area of $13' \times 13'$, we could measure $\alpha$-index for 1065 stars and the same is plotted against $(R - I)$ colors in Figure 3. We estimated a mean $\alpha$-index iteratively for these stars by 3-sigma clipping. Seven such iterations resulted in a constant mean value of 0.097 mag and a RMS scatter ($\sigma$) of 0.116 mag. Stars having $\alpha$-index within $3\sigma$ are therefore considered as having normal strength at H$\alpha$ feature. A star is considered as H$\alpha$ emitter if $\alpha \leq -0.25$ mag and H$\alpha$ absorber if $\alpha \geq 0.44$ mag. The observed characteristics of stars with H$\alpha$ emission are given in Table 6. H$\alpha$ emission stars reported only by others in the literature are also listed in Table 6. This could be due to the variable nature of H$\alpha$ emission from the stars.

We detect 29 H$\alpha$ emission-line stars, and along

**Table 6.** Photometric properties of 44 Hα emission-line stars in $13' \times 13'$ region around NGC 7419 are tabulated. Columns 1-9 are taken from the present work. Column (10) carry comments on the stars identified in the present and previous work – 'Yes' stands for detection and 'No' for non-detection in the present work, 'BMD' for Beauchamp, Moffat & Drissen (1994), 'PK' for Pigulski & Kopacki (2000), 'Sub' for Subramaniam et al. (2006) along with their identification in braces. Stars located outside the cluster region (see §2.4) are indicated with 'field'.

| ID | RA$_{J2000}$ (h m s) | DEC$_{J2000}$ (° ′ ″) | X (pixel) | Y (pixel) | V (mag) | R (mag) | α-index (mag) | R − I (mag) | Remark |
|----|----|----|----|----|----|----|----|----|----|
| (1) | (2) | (3) | (4) | (5) | (6) | (7) | (8) | (9) | (10) |
| 12 | 22 54 14 | 60 48 39 | 541.2 | 549.5 | 13.75 | 12.63 | −0.36 | +1.08 | Yes, BMD(389), PK, Sub(M) |
| 15 | 22 54 39 | 60 47 24 | 454.5 | 310.5 | 13.93 | 12.96 | −0.01 | +0.97 | No, BMD(1129), PK |
| 18 | 22 54 26 | 60 49 02 | 576.0 | 442.9 | 14.12 | 13.15 | −0.10 | +0.96 | No, BMD(781), PK, Sub(C) |
| 19 | 22 54 20 | 60 49 52 | 639.5 | 496.0 | 14.14 | 13.05 | −0.40 | +1.05 | Yes, BMD(620), PK, Sub(G) |
| 20 | 22 54 15 | 60 49 50 | 634.7 | 545.2 | 14.14 | 13.11 | −0.18 | +1.03 | No, BMD(417), PK, Sub(J) |
| 21 | 22 54 23 | 60 50 04 | 656.1 | 473.7 | 14.20 | 13.07 | −0.38 | +1.10 | Yes, BMD(702), PK, Sub(4) |
| 23 | 22 54 23 | 60 49 53 | 642.3 | 475.6 | 14.23 | 13.09 | −0.56 | +1.07 | Yes, BMD(692), PK, Sub(3) |
| 27 | 22 54 20 | 60 48 36 | 539.0 | 499.1 | 14.36 | 13.33 | −0.21 | +1.02 | No, BMD(585), PK, Sub(I) |
| 29 | 22 54 37 | 60 48 36 | 547.6 | 335.7 | 14.39 | 13.23 | −0.50 | +1.10 | Yes, BMD(1076), PK, Sub(A) |
| 38 | 22 54 27 | 60 48 52 | 564.0 | 428.1 | 14.88 | 13.76 | −0.54 | +1.04 | Yes, BMD(831), PK, Sub(B) |
| 39 | 22 54 20 | 60 48 54 | 563.3 | 492.1 | 14.93 | 13.92 | −0.05 | +1.04 | No, BMD(621), PK, Sub(K) |
| 48 | 22 54 18 | 60 48 57 | 566.2 | 517.2 | 15.14 | 14.08 | −0.50 | +1.01 | Yes, BMD(504), PK, Sub(L) |
| 57 | 22 54 26 | 60 49 05 | 581.2 | 435.0 | 15.37 | 14.30 | −0.24 | +0.81 | No, BMD(815), PK, Sub(2) |
| 59 | 22 54 08 | 60 50 23 | 673.6 | 621.9 | 15.44 | 14.18 | −0.55 | +1.20 | Yes, BMD(239), PK, Sub(5) |
| 64 | 22 54 16 | 60 47 49 | 476.0 | 532.4 | 15.54 | 14.32 | −0.57 | +1.16 | Yes, BMD(427), PK, Sub(N) |
| 66 | 22 54 14 | 60 46 20 | 358.0 | 543.2 | 15.56 | 14.51 | −0.22 | +1.13 | No, BMD(375), Sub(P) |
| 69 | 22 54 24 | 60 49 31 | 613.6 | 463.4 | 15.70 | 14.69 | −0.44 | +0.97 | Yes, BMD(728), PK, Sub(D) |
| 71 | 22 54 20 | 60 48 51 | 559.3 | 500.3 | 15.71 | 14.76 | −0.08 | +0.96 | No, BMD(582), PK, Sub(H) |
| 73 | 22 54 32 | 60 47 57 | 494.2 | 374.4 | 15.72 | 14.65 | +0.04 | +1.15 | No, BMD(967), PK |
| 74 | 22 54 10 | 60 49 39 | 617.3 | 595.2 | 15.73 | 14.67 | +0.06 | +0.59 | No, BMD(290), PK |
| 75 | 22 54 29 | 60 49 08 | 586.1 | 408.3 | 15.78 | 14.68 | −0.52 | +1.06 | Yes, BMD(884), PK, Sub(1) |
| 81 | 22 54 17 | 60 48 23 | 520.3 | 526.5 | 15.95 | 14.98 | −0.02 | +0.99 | No, BMD(451), PK |
| 85 | 22 54 17 | 60 48 18 | 514.4 | 524.8 | 15.97 | 14.93 | +0.05 | +1.06 | No, BMD(458), PK |
| 89 | 22 54 15 | 60 51 22 | 755.0 | 556.0 | 16.01 | 14.92 | −0.55 | +1.06 | Yes, Sub(Q) |
| 91 | 22 54 13 | 60 50 09 | 658.0 | 572.1 | 16.06 | 15.00 | −0.01 | +1.13 | No, BMD(351), PK |
| 95 | 22 54 17 | 60 51 37 | 776.5 | 535.6 | 16.11 | 15.10 | −0.47 | +1.01 | Yes, Sub(R) |
| 110 | 22 54 26 | 60 47 57 | 491.7 | 435.1 | 16.35 | 15.28 | −0.36 | +1.04 | Yes, BMD(795), PK, Sub(6), |
| 126 | 22 54 12 | 60 48 33 | 532.6 | 569.7 | 16.50 | 15.43 | −0.01 | +1.13 | No, BMD(340), PK |
| 127 | 22 54 19 | 60 48 14 | 509.7 | 506.9 | 16.50 | 15.45 | −0.08 | +1.11 | No, BMD(551), PK |
| 139 | 22 54 24 | 60 47 36 | 462.8 | 450.1 | 16.65 | 15.43 | −0.51 | +1.15 | Yes, BMD(745), Sub(E) |
| 145 | 22 54 07 | 60 48 17 | 508.8 | 618.9 | 16.71 | 15.33 | −0.29 | +1.33 | Yes |
| 181 | 22 54 51 | 60 48 27 | 543.4 | 199.9 | 17.07 | 15.95 | −0.28 | +1.21 | Yes, field |
| 218 | 22 54 24 | 60 47 01 | 416.6 | 447.5 | 17.32 | 16.17 | −0.40 | +1.12 | Yes, BMD(741), PK, Sub(F) |
| 321 | 22 54 13 | 60 50 27 | 681.9 | 572.7 | 18.13 | 16.92 | −0.32 | +1.23 | Yes, BMD(352), |
| 438 | 22 54 38 | 60 52 10 | 829.5 | 331.6 | 18.81 | 17.55 | −0.30 | +1.36 | Yes, field |
| —† | 22 53 33 | 60 45 51 | 300.2 | 938.4 | 18.87 | 17.27 | −0.28 | +2.11 | Yes, field |
| 655 | 22 54 56 | 60 47 41 | 485.2 | 148.1 | 19.53 | 18.14 | −0.46 | +1.58 | Yes, field |
| 703 | 22 53 37 | 60 53 22 | 895.1 | 925.5 | 19.65 | 18.45 | −0.26 | +1.24 | Yes, field |
| 714 | 22 54 40 | 60 49 24 | 612.6 | 306.4 | 19.68 | 18.40 | −0.35 | +1.44 | Yes, BMD(1157) |
| 716 | 22 54 57 | 60 53 38 | 954.5 | 157.8 | 19.68 | 18.37 | −0.32 | +1.42 | Yes, field |
| 791 | 22 55 05 | 60 53 02 | 911.0 | 82.3 | 19.90 | 18.52 | −0.43 | +1.51 | Yes, field |
| 801 | 22 54 34 | 60 51 19 | 760.3 | 366.9 | 19.92 | 18.59 | −0.32 | +1.47 | Yes |
| 808 | 22 54 40 | 60 48 31 | 542.9 | 303.1 | 19.94 | 18.70 | −0.26 | +1.26 | Yes, BMD(1153) |
| 831 | 22 54 13 | 60 45 59 | 329.3 | 553.2 | 20.01 | 18.45 | −0.48 | +1.78 | Yes |

Notes: † – Error in Vmagnitude is greater than 0.1 mag.

with 15 more reported by Pigulski & Kopacki (2000) and Subramaniam et al. (2006), the total number of Hα emission-line stars in the $13' \times 13'$ region around the cluster have now increased to 44. Of these, thirteen are newly identified in the present work. Though some late-type dwarfs do show strong chromospheric Hα in emission, but a few false detection may not be ruled out. As a non-emission late-type star generally has a series of strong metal oxide absorption lines, such as TiO in its spectrum and this may lead

to an under-estimation of their continuum, hence making the star an Hα emitter (e.g. Huang, Chen & Hsiao 2006).

## 3   PROPERTIES OF THE CLUSTER

### 3.1   Radial density profile

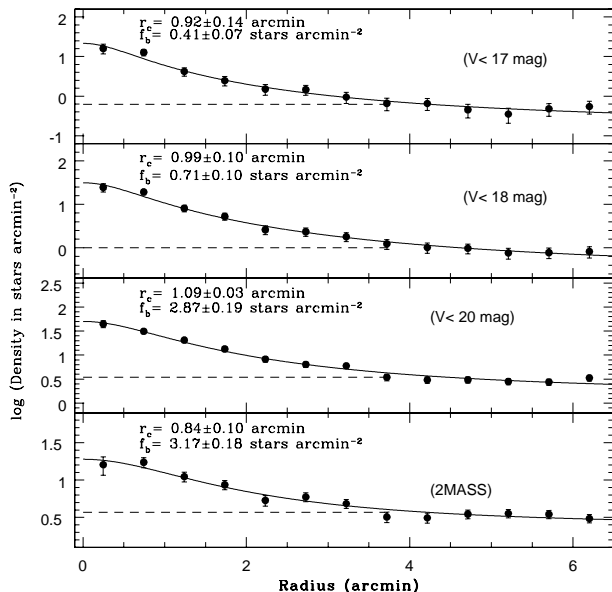We estimate the cluster center iteratively by calculating average X and Y positions of stars with $V \leq 18.0$ mag

**Figure 4.** Projected radial stellar density profile of NGC 7419. Dashed lines represent $3\sigma$ levels above the field star density and solid curve shows best fit to the empirical model of King (1962).

within 80 pixels from eye estimated center, until it converged to a constant value. The coordinates of the cluster center are found to be $RA_{J2000} = 22^h54^m18^s$ and $DEC_{J2000} = +60°48'58''$. Using this method, a typical error expected in locating the center is $5''$. To estimate extent of the cluster, we divide the cluster region into a number of concentric circles with an annulus of width $30''.5$. The projected radial stellar density profile is plotted in Figure 4 for three magnitude limits – e.g. $V = 17, 18, 20$ mag. The error bars denote Poisson statistics. The $\rho(r)$ is parameterized as (King 1962; Kaluzny & Udalski 1992)

$$\rho(r) \propto \frac{f_0}{1 + (r/r_c)^2} \qquad (1)$$

where $r_c$ and $f_0$ are the core radius of the cluster and central star density, respectively. As the observed area ($13' \times 13'$) is large compared to the cluster diameter, we estimate $f_b$ using outer region ($r > 5'$) of the cluster and to derive $f_0$ and $r_c$, we performed a Levenberg-Marquardt non-linear fitting routine (Press et al. 1992) to equation 1. The fitted parameters are shown in Figure 4. We define extent of the cluster ($r_{cl}$) as the radius at which $\rho(r)$ equals $3\sigma$ level above the field star density. Using optical data, we have estimated the core radius of about $1'$ and cluster radius of $4'.0 \pm 0'.5$ for the cluster. This is also supported by the radial density profile fits at 2MASS K-band data. The catalogue of open cluster by Dias et al. (2002) have been reported the radius of the cluster as $2'.5$. To reduce the effect of field star contamination, we therefore, consider lower limit of radius as $3'.5$ for further analysis.

### 3.2 Color-magnitude diagrams

The $V, (U-B)$; $V, (B-V)$ and $V, (V-I)$ color-magnitude diagrams (CMDs) of the cluster region along with $V, (V-I)$ CMD of the field region are shown in Figure 5. Morphology of the CMDs is typical of a young-age open star clus-

ter and the main sequence extends down to $V \sim 22.0$ mag in $V, (V-I)$ CMD. It is seen that the field star contamination becomes more evident for stars with $V > 18$ mag, therefore, a statistical criteria was used to remove the field star contamination, following procedure adopted by Sandhu, Pandey & Sagar (2003). For this purpose, we assume a uniform distribution of field stars in an area outside the cluster region ($r > 3'.5$). The luminosity function (LF) derived from the $V, (V-I)$ CMD of the field region was subtracted from the LF of the cluster region. For a randomly selected star in the $V, (V-I)$ CMD of field region, the nearest star in the $V, (V-I)$ CMD of cluster region within $V \pm 0.25$ mag and $(V-I) \pm 0.125$ mag of the field star was removed. The necessary corrections for CF have also been considered in statistical subtraction. Statistical subtraction of data have been done till $V \approx 21.0$ mag only as they have CF value $> 0.5$. The $V, (V-I)$ diagram of statistically cleaned cluster sample is shown in Figure 5. Further, to select main-sequence members more reliably, we define blue and red envelope in statistically cleaned CMD and the same is shown in the left panel of Figure 6.

### 3.3 Interstellar reddening

#### 3.3.1 Law of interstellar reddening

We investigated the nature of interstellar reddening towards the cluster direction using the color excess ratio method as described by Johnson (1968). We select stars with spectral types earlier than A0 by applying criterion of $V < 17.7$ and $1.35 < (B-V) < 1.70$ on probable members of the cluster (§3.2). From this list we exclude stars showing either $H\alpha$ emission (see§2.4) or NIR excess (see§4) as their reddening properties are likely to be different from the normal stars Kumar et al. (2004). We estimate intrinsic colors using Q-method (cf. Johnson & Morgan 1953) and iteratively estimate reddening free parameter Q $[= (U-B) - X(B-V)$, where $X = E(U-B)/E(B-V)]$, till the color excess ratios become constant within the photometric errors. For the first iteration, we assume $X = 0.72$. The color excesses are determined using intrinsic colors as derived from the MKK spectral type-luminosity class color relation given by Caldwell et al. (1993) for $(U-B)$, $(B-V)$, $(V-R)$ and $(V-I)$ and by Koornneef (1983) for $(V-J)$, $(V-H)$ and $(V-K)$. Mean values of color excess ratios derived for the cluster are given in Table 7 and except $X$, all other color excess ratios are in agreement with that expected for normal interstellar matter (Cardelli, Clayton & Mathis 1989). The value of $X$ ($\sim 0.90 \pm 0.08$) is significantly greater than the normal value of $\sim 0.72$, which implies that the average dust grain sizes are smaller than average. The ratio of total-to-selective extinction is estimated using the relation $R_V = 1.1E(V-K)/E(B-V)$ (Whittet & van Breda 1980) and it is found to be $3.2 \pm 0.1$.

We have also determined the value of color excess ratios using our $UBVRI$ photometry and spectral classification of six stars (see Table 8) available in the literature (Caron et al. 2003; Beauchamp, Moffat & Drissen 1994). Intrinsic colors [3] are read from Wegner (1994) for $(V-R)$ and $(V-I)$,

---

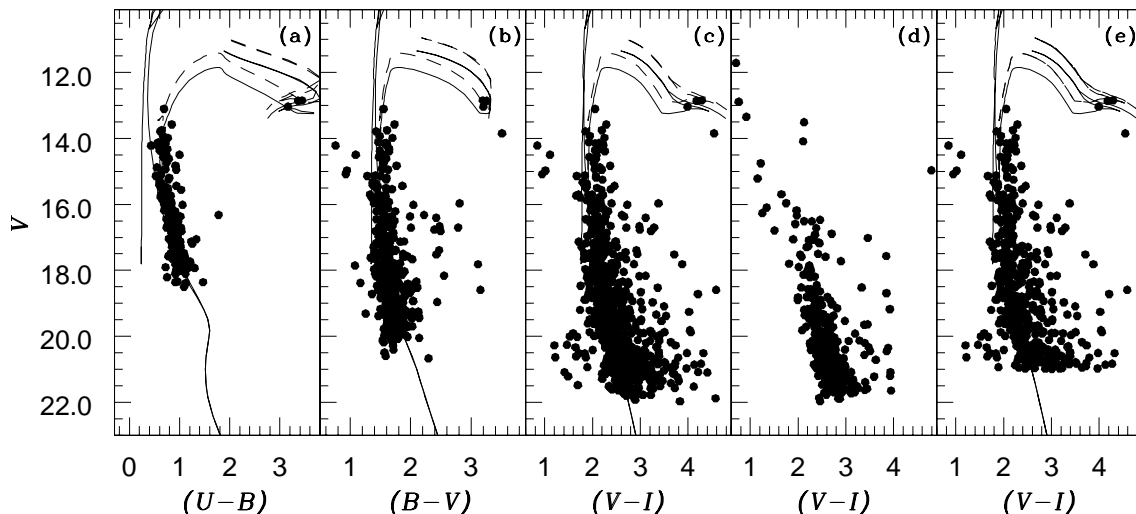[3] The intrinsic colors of Johnson $RI$ in Wegner (1994) are con-

**Figure 5.** Color-magnitude diagrams for cluster regions are shown in panels (a) $V, (U-B)$ (b) $V, (B-V)$ and (c) $V, (V-I)$. Panel (d) is for field region and the statistically cleaned $V, (V-I)$ CMD for cluster is shown in panel (e). Theoretical isochrones from GRD02 are shown with continuous lines for log(age)= 6.6, 7.3 and 7.4 Myr in the panels (a), (b), (c) and (e).

**Table 7.** Observed color excess ratios in the direction of NGC 7419 are listed along with the excess ratios valid for normal interstellr reddening law, $R_V$=3.1 (Cardelli, Clayton & Mathis 1989).

| Object | $\frac{E(U-B)}{E(B-V)}$ | $\frac{E(V-R)}{E(B-V)}$ | $\frac{E(V-I)}{E(B-V)}$ | $\frac{E(U-B)}{E(V-J)}$ | $\frac{E(B-V)}{E(V-J)}$ | $\frac{E(V-R)}{E(V-J)}$ | $\frac{E(V-I)}{E(V-J)}$ | $\frac{E(V-H)}{E(V-J)}$ | $\frac{E(V-K)}{E(V-J)}$ |
|---|---|---|---|---|---|---|---|---|---|
| NGC 7419 | 0.90±0.09 | 0.62±0.02 | 1.29±0.04 | 0.37±0.04 | 0.41±0.01 | 0.25±0.01 | 0.52±0.01 | 1.14±0.01 | 1.20±0.02 |
| Normal value | 0.72 | 0.62 | 1.25 | 0.32 | 0.43 | 0.27 | 0.56 | 1.13 | 1.21 |

from Fitzgerald (1970) for $(U - B)$. The mean value of $X$ $(= 0.88 \pm 0.06)$ using this method is in good agreement with the one derived from iterative Q-method. Further, the excess ratios at other wavebands, and mean value of $R_V$ ($= 3.16 \pm 0.10$) are also close to the one derived using Q-method (see Table 8).

Higher value of color excess ratio $X$, as found above, is also supported by the $V, (U - B)$ CMD (Figure 5), in which the isochrones (Girardi et al. 2002, hereafter GRD02) are found to fit well with $X = 0.90$. Such anomalous values of $X$ are not uncommon for the interstellar matter in the Milkyway and a higher value of $X(> 0.72)$ has also been reported along lines of sight of other star forming clusters, for example, NGC 869 ($X = 0.90$; Pandey et al. 2003); Markarian 50 ($X = 0.81$; Baume, Vázquez & Carraro 2004) and NGC 7510 ($X = 0.78$; Barbon & Hassan 1996) However, they report normal value for other color excesses in these clusters. For further analysis, we have therefore used the normal value of color excess ratios except for the value $E(U - B)/E(B - V)$, which is adopted as 0.90.

### 3.3.2 Determination of reddening

Figure 7 shows observed color-color, $(U - B), (B - V)$, diagram for the cluster region. To determine reddening $E(B - V)$, the intrinsic colors for main-sequence stars with solar metallicity (Schmidt-Kaler 1982) are reddened along
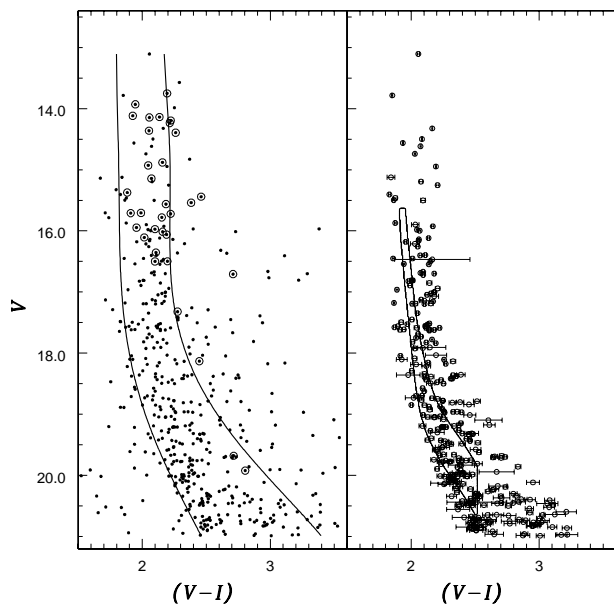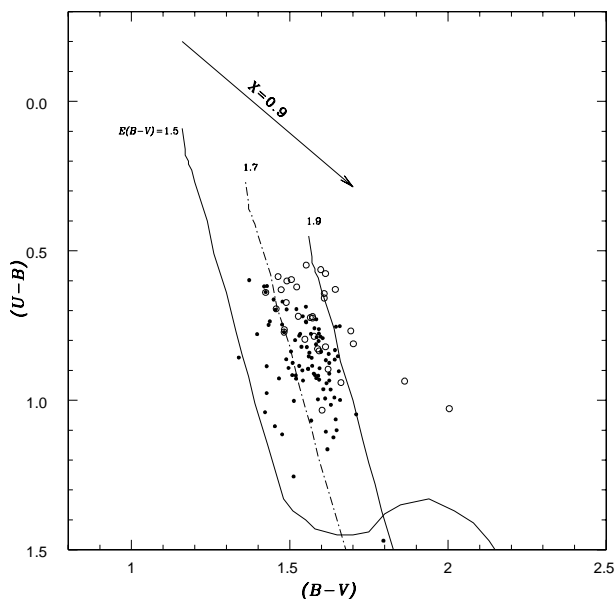


**Figure 6.** Statistically cleaned $V, (V - I)$ CMD for NGC 7419. *Left panel:* Solid lines confine the blueward and redward boundary of the main-sequence. Emission line stars are encircled. *Right panel:* Solid curves show the best fit Padova isochrone obtained using $\tau^2$-minimization method (Naylor & Jeffries 2006) for fixed z=0.019 and age =25 Myr with distance as free parameter. Horizontal bars denote errors in $(V - I)$. See §3.5 for further details.

verted into Cousins $RI$ using Bessell (1979) transformation relations.

**Table 8.** Giant stars with known spectral types in the literature (Caron et al. 2003; Beauchamp, Moffat & Drissen 1994). Color excess ratios are derived using present data.

| ID | BMD ID | Spectral Type | E(B-V) | $\frac{E(U-B)}{E(B-V)}$ | $\frac{E(V-R)}{E(B-V)}$ | $\frac{E(V-I)}{E(B-V)}$ | $\frac{E(V-K)}{E(B-V)}$ | $R_V = 1.1\frac{E(V-K)}{E(B-V)}$ |
|----|--------|---------------|--------|-------|-------|-------|-------|-------|
| 8  | 687  | B2.5 II  | 1.741 | 0.883 | 0.641 | 1.283 | 2.924 | 3.216 |
| 13 | 473  | B2.5 III | 1.648 | 0.891 | 0.623 | 1.245 | 2.754 | 3.030 |
| 15 | 1129 | B4.0 III | 1.669 | 0.752 | 0.639 | 1.266 | 2.833 | 3.116 |
| 16 | 190  | B0.0 III | 1.999 | 0.924 | 0.642 | 1.267 | 2.837 | 3.120 |
| 20 | 417  | B1/2 III | 1.845 | 0.912 | 0.638 | 1.263 | 2.903 | 3.193 |
| 12 | 389  | B1/2 III | 1.789 | 0.896 | 0.670 | 1.313 | 3.014 | 3.315 |



**Figure 7.** The $(B-V), (U-B)$ color-color diagram for stars in the cluster region. Open circles represent stars with H$\alpha$ emission. Solid lines are intrinsic main-sequence reddened along the reddening line with $E(B-V) = 1.5$ mag and 1.9 mag, while the dotted line is for 1.7 mag.

the reddening vector $(X = 0.9)$. This reddened main-sequence suggests that $E(B-V)$ for the cluster region varies from 1.5 to 1.9 mag, with a visual mean value of about 1.7 mag. This reddening variation ($\sim 0.4$ mag) for cluster members is well above the typical width of intrinsic main-sequence stars i.e. $\leq 0.11$ mag, which is caused usually due to photometric accuracy and the presence of binary stars (Sagar et al. 1987). It therefore indicates the presence of variable reddening within the cluster region, which is also reported by Subramaniam et al. (2006). Few emission-line stars (open circles) are found to have $E(B-V) > 1.9$ mag and these may either be embedded deep in the parent cloud or be surrounded with circumstellar matter. Using iterative Q-method (§3.3.1), we derive mean value of $E(B-V)$ as $1.7 \pm 0.2$ mag, which is same as estimated visually by color-color diagram, and hence we adopt this value in our further analysis.

### 3.4   Turn-off age of the cluster

Turn-off age of the cluster is determined by comparing the theoretical stellar evolutionary models, the Padova

isochrones GRD02 for solar metallicity Z=0.019 with observed CMDs (see Figure 5). Theoretical isochrones for ages 4, 20 and 25 Myr, corrected for the mean reddening $E(B-V) = 1.7$ mag, are shown with solid lines and are visually fitted to the bluest envelope of CMDs consisting of probable members as selected in §3.2. It is found that $X = 0.9$ results in a better isochrone fit in $V, (U-B)$ CMD than the normal value, $X = 0.72$ (§3.3.1). Locations of the red supergiants (Caron et al. 2003) BMD 921 (M2.5Iab), BMD 696 (M2.5Iab) and BMD 435 (M2.5Iab) are found to be consistent with the isochrones, while BMD 139 (M3.5I) and BMD 950 (M7.5), both pulsating supergiants were prone to produce more scatter in distance and age estimate of NGC 7419. Thus, using the visual-fit method, the present data finds the turn-off age of the cluster to lie between 19 Myr to 25 Myr and hence we assign an age of $22.5 \pm 2.5$ Myr.

We also estimate age using morphological age method (Phelps, Janes & Montgomery 1994; Pandey et al. 1997), which employes color-index parameter (CIP), defined as the difference in the color index between the blue turnoff point of the main-sequence and the color at the base of the red giant branch. For NGC 7419, CIP is calculated as 1.654 mag and it represents the age between 20 and 25 Myrs, which is in good agreement with our previous value. The present age estimate is similar to the one derived by Subramaniam et al. (2006) less than the 50 Myr given by Bhatt et al. (1993) and older than 14 Myr derived by Beauchamp, Moffat & Drissen (1994).

### 3.5   Distance to the cluster

The zero-age main-sequence fitting procedure (Figure 5) is used to derive the distance of the cluster and the distance modulus is estimated as $12.45 \pm 0.20$ mag which corresponds to a distance of $3100 \pm 290$ pc. The distance determination is further performed using a maximum likelihood $\tau^2$-minimization method which employs fitting two-dimensional distributions to stellar data in color magnitude space (Naylor & Jeffries 2006; Mayne et al. 2007; Jeffries et al. 2007). This takes into account the effects of binary population as well as observed photometric errors. Assuming an age of $\sim 22.5$ Myr and a binary fraction of 0.5, the best-fit Padova isochrone with solar metallicity yields a distance modulus of 12.55 mag (Figure 6,§3.2). Emission-line stars were excluded from this fit. Adding a systematic error of 0.28 mag due to differential reddening to each data point would result $P_r(\tau^2) = 0.5$ with 68% confidence ranges from 12.24 to 12.76 mag. We, therefore adopt a distance of $3230^{+330}_{-430}$ pc for NGC 7419, which is similar to the es-

timate of Subramaniam et al. (2006) but higher from the value reported by Beauchamp, Moffat & Drissen (1994) and Bhatt et al. (1993).

## 4 NEAR-INFRARED DATA AND INTERMEDIATE MASS STARS

To understand the global scenario of star formation around NGC 7419, we use NIR $JHK_s$ data for point sources within a square degree region centered on $RA_{J2000} = 22^h52^m28^s$ and $DEC_{J2000} = +60°53'52''$, which is $14'.23$ west from the cluster center. It contains the entire cluster and the surrounding star forming region. Data have been obtained from the 2MASS Point Source Catalog (PSC) (Cutri et al. 2003). We have selected the sources based on the 'read-flag' which gives the uncertainties in the magnitudes. We retain 2MASS sources with 'read flag' values of 1-2 for good quality data in our analysis. The $JHK_s$ colors were transformed from 2MASS system to California Institute of Technology system using the relations given on the 2MASS web site [4].

### 4.1 Color-color diagrams

The $(J - H), (H - K)$ color-color diagram is plotted for the cluster region (471 stars) and the surrounding square degree region (22100 stars), in Figures 8. Solid lines represent unreddened main-sequence and giant branch (Bessell & Brett 1988). The parallel solid lines are the reddening vectors for early and late-type stars (drawn from the base and the tip of two branches). Location of T-Tauri stars (TTS; Meyer, Calvet & Hillenbrand 1997), proto-star (PS) like objects, classical Be stars and Herbig Ae/Be (Dougherty et al. 1994; Hernandez et al. 2005) are also shown. The extinction ratio $A_J/A_V = 0.282$, $A_H/A_V = 0.180$ and $A_K/A_V = 0.116$ have been taken from Cardelli, Clayton & Mathis (1989). Stars below the reddening vectors are considered to have NIR excess. The asterisks represent all the stars with H$\alpha$ emission (Table 6). Of 44 emission-line stars only 39 stars have NIR counterparts within $3''$. NIR excess is shown by 17 emission-line stars within the cluster region but 4 more emission-line stars are situated at the boundary of the reddening vector, therefore they have also considered as NIR excess stars within error bars in colors. From spectroscopic studies, Subramaniam et al. (2006) have identified them as Herbig Ae/Be stars. Therefore, NGC 7419 is a peculiar cluster having such a large number of Herbig Ae/Be stars. In surrounding region, 90 sources are found in the T-Tauri locus (Meyer, Calvet & Hillenbrand 1997). These sources are considered to be mostly classical T-Tauri stars (Class II objects) with large NIR excesses and belong to the YSO population. There may be an overlap in NIR colors of Herbig Ae/Be stars and T-Tauri stars in the TTS region (Hillenbrand et al. 1992). Such a large number of young stars represent the youth of this region. But all the T-Tauri stars with NIR excesses are situated outside the cluster region.
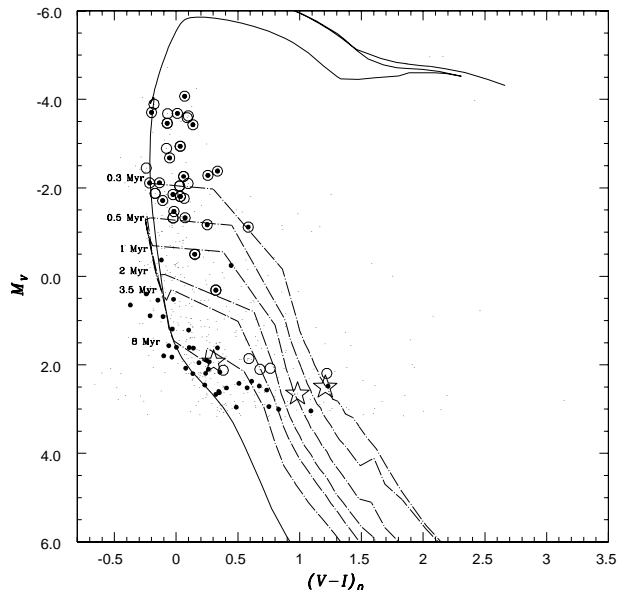
---

[4] http://www.astro.caltech.edu/~jmc/2mass/v3/transformations/



**Figure 9.** Color-magnitude diagram $M_V, (V - I)_0$ of the cluster region. Open circles denote stars with H$\alpha$ emission (Table 6), asterisks denote stars with X-ray counterparts and having membership probability from X-ray colors while filled dots represent stars with NIR excess. Post-main-sequence isochrone for 25 Myr by GRD02 (continuous line) and pre-main-sequence isochrones for 0.3, 0.5, 1, 2, 4, 8 Myr by SES00 (dashed lines) are also shown. Isochrones are corrected for a distance of 3.23 kpc.

### 4.2 Cluster Age from Herbig Ae/Be stars

Figure 9 shows $M_V, (V - I)_0$ color magnitude diagram for H$\alpha$ emission stars (open circles; Table 6), NIR excess stars (black dots), stars with X-ray counterpart (asterisks; §8.3). Star BMD 950 is not shown as it shows a large error (> 0.1 mag) in $I$ band. It is seen that most of Herbig Ae/Be stars are located to the right side of the main-sequence and to estimate their age, we use pre-main-sequence isochrones from Siess, Dufour & Forestini (2000), hereafter SES00, for ages 0.3, 0.5, 1, 2, 4 and 8 Myr, shown with dashed lines in Figure 9. For reference, the post-main-sequence isochrone of 25 Myr age GRD02 have been shown by continuous lines. Only one X-ray source and three emission-line star lie in the range of 3.5–8 Myr isochrones, which may arise due to field star contamination of the Herbig Ae/Be stars loci in the NIR color-color diagram (Figure 8). Therefore, considering only the large number of Herbig Ae/Be stars, i.e. emission-line stars with NIR excess, it is very likely that the turn-on age of the cluster cannot be more than 2 Myr.

### 4.3 Mass of Herbig Ae/Be stars using NIR color-magnitude diagram

Stellar masses are determined using NIR color-magnitude $J, (J - H)$ diagram. We prefer $J$ over $H$ or $K$, as the $J$ waveband is less affected by the emission from circumstellar material (Bertot, Basri & Bouvier 1988). Left panel of Figure 10 shows NIR CMD for the cluster region NGC 7419. The 4 Myr post-main-sequence isochrone GRD02 and pre-main-sequence evolutionary tracks for mass range $2 - 7M_\odot$ SES00 are plotted assuming a distance of 3.2 kpc and a mean
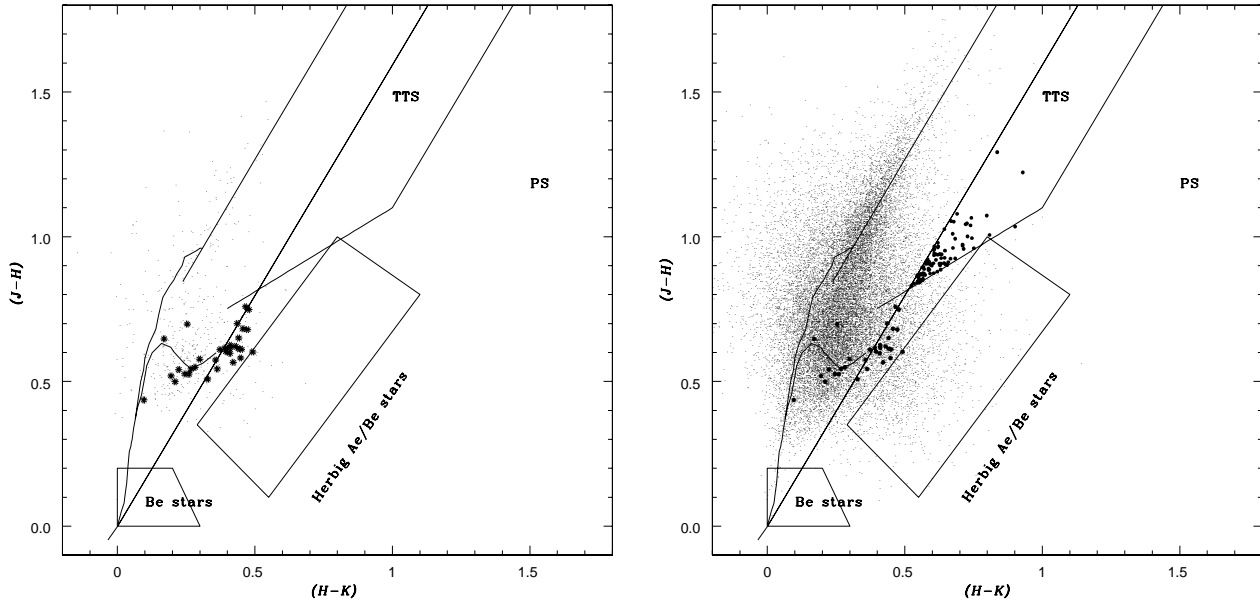
**Figure 8.** Color-color diagrams using the 2MASS JHK data. *left panel:* The NIR color-color diagram for the cluster region NGC 7419. Small dots represent the NIR stars present in cluster region and the asterisks denote the Hα emission-line stars from Table 6. *right panel* : Same as the left panel, but for the square degree surrounding region centered at $RA_{J2000} = 22^h52^m28^s$ and $DEC_{J2000} = +60°53'52''$. Bigger filled dots denote 90 T-Tauri stars in this region.
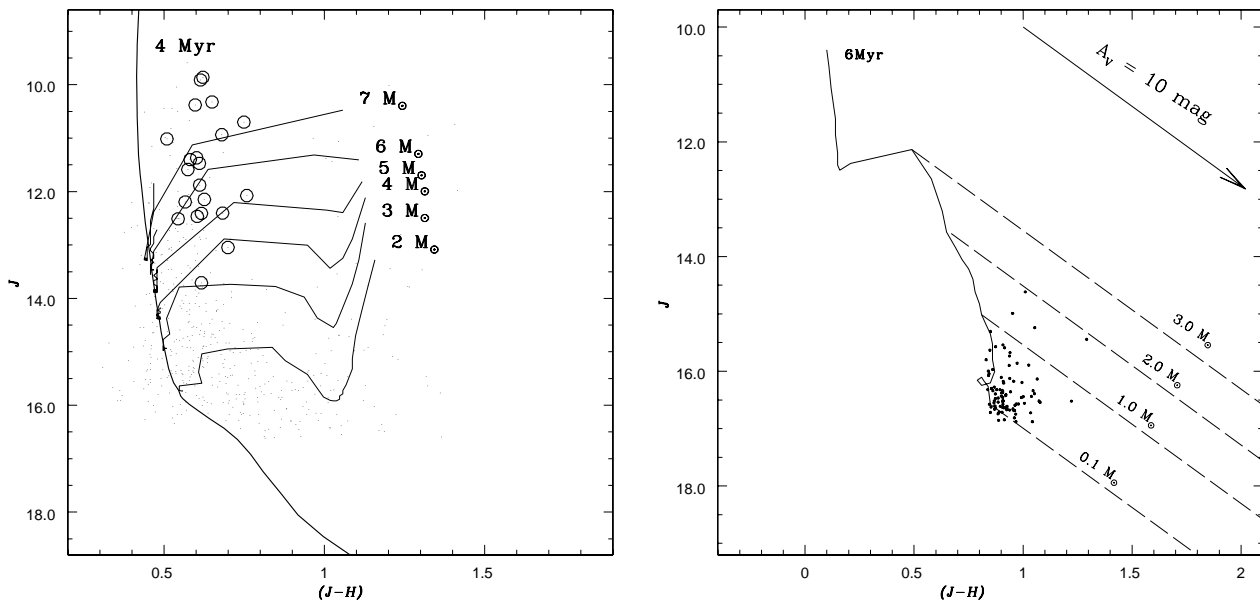


**Figure 10.** Stellar mass estimate using NIR CMD diagram. *left panel: J, (J − H)* CMD for Herbig Ae/Be stars in the cluster region NGC 7419 are shown with open circles. The 4 Myr post-main-sequence isochrone GRD02 and the pre-main-sequence evolutionary tracks for masses $2 − 7M_⊙$ are also shown and indicated. *right panel:* Same as left panel but for the YSO candidates (asterisks) in the surrounding square degree region of NGC 7419. Solid curve denotes pre-main-sequence isochrone of 6 Myr SES00, while the dashed oblique reddening lines denote the positions of pre-main-sequence stars for masses 0.1, 1, 2 and $3M_⊙$.

reddening $E(B − V)$ of 1.70 mag (§3.3,§3.5). Reddening and extinction corrections to the isochrone and tracks are made using the relation $A_J/A_V = 0.282$ and $A_{(J−H)}/A_V = 0.102$ (Cardelli, Clayton & Mathis 1989), where $A_V = 3.1E(B − V)$. Location of 21 Herbig Ae/Be stars in NIR CMD is represented by open circles and it is seen that 66% of these are located between the mass range $5 − 7M_⊙$. Only two stars lie in the mass range $3 − 4M_⊙$.

Right panel of Figure 10 represents NIR CMD for 90 probable YSO candidates (shown with filled circles) identified in a square degree region around the cluster (Figure 8). None of these YSOs are present in the cluster region and hence we argue that the population of YSOs is most likely associated with a local arm molecular cloud sh2-154 (Ungerechts et al. 2000), see §5 for detailed discussion. We, therefore, correct the theoretical isochrones

**Table 9.** IRAS point sources present in the square degree region centered about $RA_{J2000} = 22^h53^m26^s$ and $DEC_{J2000} = +60°53'52'$. ID 44 is a carbon star.

| ID | IRAS PSC | $F_{12}$ (Jy) | $F_{25}$ (Jy) | $F_{60}$ (Jy) | $F_{100}$ (Jy) | Remark |
|----|----------|------|------|------|-------|--------|
| – | 22493+6018 | 7.04 | 2.39 | 3.12 | 48.91 | VMW Cep |
| 42 | 22527+6030 | 2.53 | 0.77 | 17.05 | 87.48 | VMZCep |
| – | 22525+6033 | 112.10 | 92.30 | 17.05 | 50.10 | M7.5Iab |
| 14 | 22520+6031 | 3.10 | 1.06 | 17.05 | 50.87 | M3.5 Iab |
| – | 22512+6100 | 108.50 | 93.30 | 16.68 | 15.27 | V386Cep |
| – | 22538+6102 | 1.04 | 0.49 | 6.50 | 70.00 | — |
| – | 22486+6028 | 0.85 | 0.37 | 4.95 | 53.07 | — |
| – | 22490+6043 | 0.54 | 0.35 | 5.35 | 39.51 | — |
| – | 22469+6053 | 0.46 | 0.25 | 5.55 | 71.76 | — |
| – | 22480+6056 | 0.30 | 0.25 | 5.34 | 68.93 | — |

**Table 10.** Same as for Table 9 except for the MSX point sources.

| ID | Name MSX PSC | $F_A$ (Jy) | $F_B$ (Jy) | $F_C$ (Jy) | Remark |
|----|--------------|------|------|------|--------|
| – | G108.6966+01.0686 | 6.70 | 5.80 | 3.72 | VMWCep |
| – | G109.1599+01.1206 | 87.83 | 133.58 | 96.95 | M7.5 Iab |
| 42 | G109.1632+01.0645 | 3.31 | 2.14 | 1.48 | VMZ Cep |
| 5 | G109.1353+01.1118 | 3.40 | 2.00 | 1.68 | M2.5 Iab |
| 4 | G109.1302+01.1321 | 3.43 | 2.11 | 1.33 | M2.5 Iab |
| 7 | G109.1445+01.0947 | 1.71 | 0.71 | 0.74 | M2.5 Iab |
| 14 | G109.0901+01.1184 | 3.38 | 2.41 | 1.58 | M3.5 Iab |
| – | G109.2152+01.6007 | 63.48 | 83.70 | 66.06 | V386Cep |

SES00, for extinction assuming the cloud distance of 1.4 kpc (Khalil, Joncas & Nekka 2004) and for reddening assuming a value of 0.4 mag/kpc towards the direction of NGC 7419 (Joshi 2005). The corrected isochrones are shown with solid curves in the right panel of Figure 10 and they trace the locus of 6 Myr pre-main-sequence stars having masses in the range $0.1 - 3M_\odot$. It is observed that masses of all of the YSOs lie in the range $0.1 - 2.0M_\odot$ indicating them to be T-Tauri stars. Therefore, almost all of the YSO candidates are low mass pre-main-sequence stars.

## 5 SPATIAL DISTRIBUTION OF LOW MASS PRE-MAIN-SEQUENCE CANDIDATES

In Figure 11, we show a square degree $R$-band image, reproduced from DSS[5], of the field containing YSO candidates and the cluster NGC 7419. Inner ($r \leq 1'$) and outer boundaries ($r \leq 3'.5$) of the cluster are encircled. Point sources from MSX (Midcourse Space Experiment) which surveyed the Galactic plane in four mid-infrared bands - A(8.28 $\mu$m), C(12.13 $\mu$m), D(14.65 $\mu$m), and E(21.34 $\mu$m) at spatial resolution of $\sim 18''$ (Price et al. 2001), are also shown in Figure 11. Information about 10 IRAS (Infra-Red Astronomical Satellite) point sources and 8 MSX point sources are given in Table 9 and Table 10, respectively. The MSX sources are denoted by white open circles while asterisks represent IRAS sources. YSO candidates are denoted by open square boxes. Of 8 MSX sources, six are identified with five supergiants and a carbon star and the other two are G108.6966+01.0686, a carbon star VMW Cep
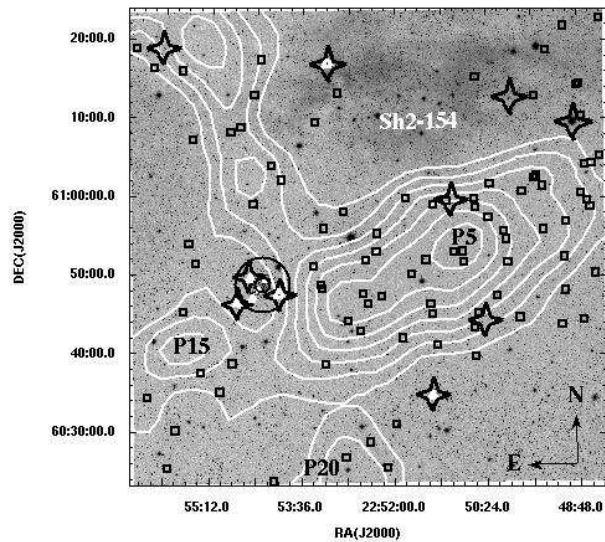


**Figure 11.** A square degree $R$-band DSS image of the field surrounding the cluster NGC 7419. North is up and east is to the left. Open boxes show the candidate YSOs, white thick dots represent MSX sources and open star symbols denote IRAS point sources. Inner ($r \leq 1'$) and outer boundaries ($r \leq 3'.5$) of NGC 7419 are encircled. The location of Sharpless nebula Sh2-154 is also marked. The dust extinction maps produced using star counting method are overlaid by white contours, and the associated clumps P5, P15 and P20 with cloud 699 are also marked (Dobashi et al. 2005).

(Kukarkin et al. 1968), and G109.2152+01.6007, a semi regular pulsating star V386 Cep (Stephenson 1984). The cluster supergiants also have IRAS counterpart, and their presence in NGC 7419 is also supported from mid-infrared data.

In the following, we describe the attenuation properties of a square degree region around the cluster (see §4). Dobashi et al. (2005) recently produced extinction maps of the entire region of the Galaxy in the galactic latitude range $b \leq 40°$ by applying traditional star count technique to the optical DSS sources. We retrieved the FITS images of the extinction map of the field containing NGC 7419 and their surrounding region from their on-line website[6]. In Figure 11, we overlay the contours of high resolution extinction map. The contours are plotted at $A_V = 2.5$ to 4.5 with an interval of 0.3 mag. The extinction towards the location of the cluster shows relatively low ($A_V \leq 2.5$) values, in comparison to the outer region of the cluster especially, towards the west, the east and the south, where extinction increases up to $\sim 4.5$, $\sim 3.2$ and $\sim 3.0$ mag, respectively. These enhanced attenuations are identified with the dense cloud clumps P5, P15 and P20 of dark cloud 699 (Dobashi et al. 2005). Using star count method it would be difficult to detect dust obscuration located at a cluster distance of $\sim$3.2 kpc, as the cloud would become inconspicuous due to large number of foreground stars (Dobashi et al. 2005; Medhi et al. 2008). We, therefore, argue that the dust obscuration would be due to a foreground cloud.

In order to see the dust emission characteristics of this cloud, we superimpose the IRAS 100 $\mu$m contours obtained from the Infrared Processing and Analysis Center (IPAC) on $R$-band DSS image in Figure 12, left panel. The IRAS survey was done in four bands 12 $\mu$m, 25 $\mu$m, 60 $\mu$m and 100 $\mu$m from mid-infrared to far-infrared. The contours are plotted after smoothing the IRAS 100 $\mu$m image. The contours are drawn at 134 (outermost) to 204 with the increment of 10 M Jy sr$^{-1}$. The IRAS dust emissions support the presence of dust obscuration at the location of cloud clumps P5, P15 and P20. The star count extinction map is seen to be highly correlated with the 100 $\mu$m IRAS dust map and represent the same morphology of the cloud. We also show the $^{12}$CO temperature map of the region, see right panel in Figure 12 (Kerton & Brunt 2003). The contours are drawn for temperature ranges $6.5 - 9.5$ K with the increment of 0.5 K. The peak of CO emission is most likely associated with clump P5 ($\sim 5.'5$ westward). A slight mismatch might be the effect of low resolution of the extinction map (Dobashi et al. 2005). It is seen that 60% of total YSO population seems to be associated with the clumpy region P5. Therefore, the clump P5 may provide a fertile environment for the formation of the low mass stars.

Interestingly, the spatial distribution of TT stars is highly correlated with the extinction and IRAS dust map (see Figure 11), it is therefore likely that the population of YSOs (§4) might be associated with the foreground dark cloud. Avedisova (2002) identify a local arm star forming region Sh2-154, situated in the north-east direction from the cluster. Optical diameter and distance of Sh2-154 is estimated respectively as 60$'$ and 1.4 kpc (Blitz, Fich & Stark 1982). Hence, the YSO population (Figure 8) could be part of Sh2-154 and associated with a dark cloud clump 699/P5 and 699/P15 as identified by Dobashi et al. (2005).

The effect of environment on the production of the low mass stars has been investigated with the help of the distribution of the reddening in the cloud by assuming that they are situated at the same distance. The $A_V$ value for each star was measured by tracing back to the intrinsic lines along the reddening vector found in Meyer, Calvet & Hillenbrand (1997). The value of $A_V$ is found to vary from 0 to 3 mag. Only one YSO has $A_V \sim 5$ mag. The spatial distribution of the $A_V$ from 0 to 5 mag is shown in Figure 13, left panel. No spatial gradient of $A_V$ is found with the spatial distribution of the YSOs. The frequency distribution of $A_V$ (Figure 13, right panel) represents that 77% YSOs are having $A_V$ less than 1.0 mag and 15% of YSOs with $A_V$ in between 1.0 to 2.0 mag. It shows that the environment for the YSOs is almost similar.

The effect of the youthfulness of the YSOs in the spatial distribution can also be investigated with the help $(H - K)_{\mathrm{excess}}$, which is expected due to the presence of the circumstellar disk dissipating with time Oasa et al. (2006). For YSOs, it is determined by the method used in Matsuyanagi (2006) and it lies in the range $0.002 - 0.3$ mag. The distribution of $(H - K)_{\mathrm{excess}}$ (Figure 14, left panel) does not show any spatial gradient with distribution of the YSOs, indicating that the YSOs having different age are distributed uniformly within the cloud. Frequency distribution of the $H - K$ excess is shown in Figure 14, right panel and it indicates that 89% of YSOs have nearly similar age. This

represents a uniform distribution of the star formation rate within the cloud.

The morphology of the cloud is almost the same for all the YSOs and we find very little age dispersion in the YSOs. There is no significant contribution of the external agents found in the formation of these YSOs in this cloud. Therefore, such a uniform distribution of YSO candidates might be the result of primordial fragmentation.

## 6   MASS FUNCTION

The initial mass function (IMF) is the distribution of stellar masses that form in a star formation event in a given volume of space. It is an important result of star formation and together with the star formation rate, the IMF dictates the evolution and fate of galaxies and star clusters (Kroupa 2002). However, the direct determination of IMF is not possible due to the dynamical evolution of stellar systems. Therefore, we derived MF which is often expressed by the power law, $N(logm) \propto m^{\Gamma}$ and the slope of the MF is given as :

$$\Gamma = dlogN(logm)/dlogm \qquad (2)$$

where $N(logm)$ is the number of star per unit logarithmic mass interval. In the solar neighborhood the classical value derived by Salpeter (1955) is $\Gamma = -1.35$. In order to estimate the MF for the cluster region, we have used statistically cleaned sample described in §3.2. We have divided statistically cleaned sample for two star formation episodes. The first star formation episode is at 25 Myr and the masses corresponding to $V \leq 21$ mag have reached to the main-sequence, therefore only main-sequence MF have been considered for this episode. In Figure 15, the MS represents the main-sequence band (selected in §3.2) and is drawn by long-dashed lines. The stars within this band are shown by solid dots. The main-sequence theoretical isochrone from GRD02 is shown by solid line at 25 Myr age with upper limit at $V \approx 15.0$ mag because the stars above this point have been evolved from the main-sequence. Due to the above mentioned reasons, we have considered the stars with $V$ magnitude ranges $15 - 21$ mag for the main-sequence MF. The second episode is at age $\leq 2$ Myr, therefore pre-main-sequence MF has been derived for the stellar population attached with this episode. The pre-main-sequence theoretical isochrones by SES00 have been drawn by solid lines for ages 2 Myr and 0.1 Myr (upper limit of age in model), and by dashed lines with dots for masses ranges from 2 $M_{\odot}$ to 7 $M_{\odot}$, respectively. The stars which are lying in between this age range have been used for the estimate of pre-main-sequence MF and shown by triangles in Figure 15. The Herbig Ae/Be stars, described in §4, are shown by open circles. All these stars are excluded in the estimation of main-sequence MF even though they are lying inside the selected MS band, and considered as pre-main-sequence stars and included in the estimation of pre-main-sequence MF. We have used the stars shown by triangles in Figure 15 and the Herbig Ae/Be stars inside the MS band for the estimation of pre-main sequence MF for masses down to $\sim 3M_{\odot}$ due to the incompleteness of mass below this limit.

We have derived the MF from LF using the theoretical evolutionary models. The MF in two subregions i.e., the in-
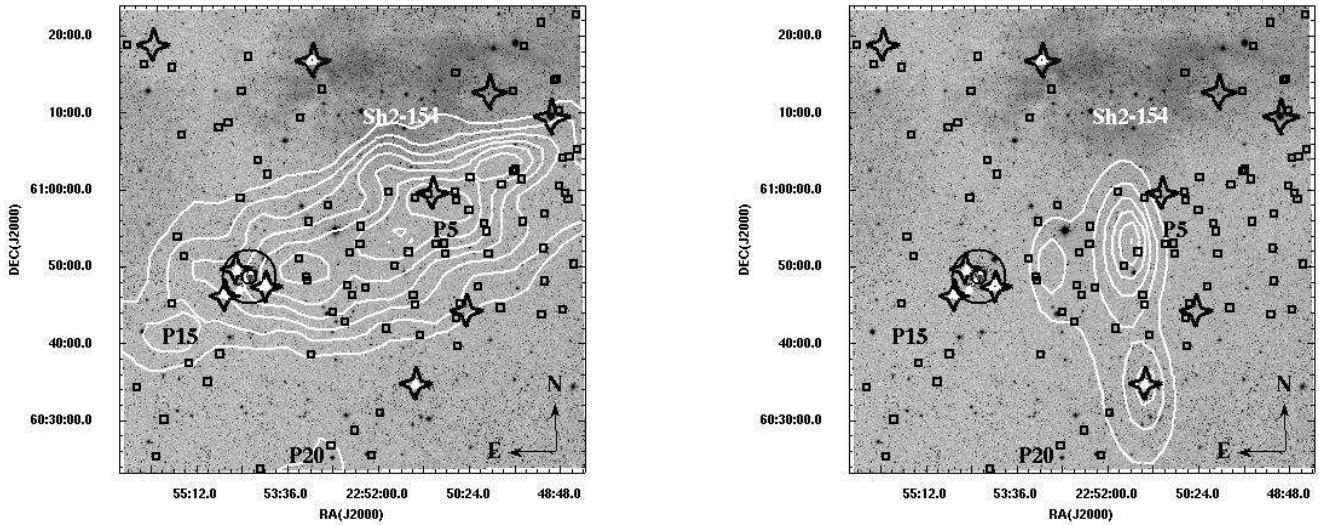
**Figure 12.** Same as Figure 11 but white counters represent in *left panel:* Contours of 100 $\mu$m IRAS dust emissions, in *right panel :* $^{12}$CO temperature map (Kerton & Brunt 2003).
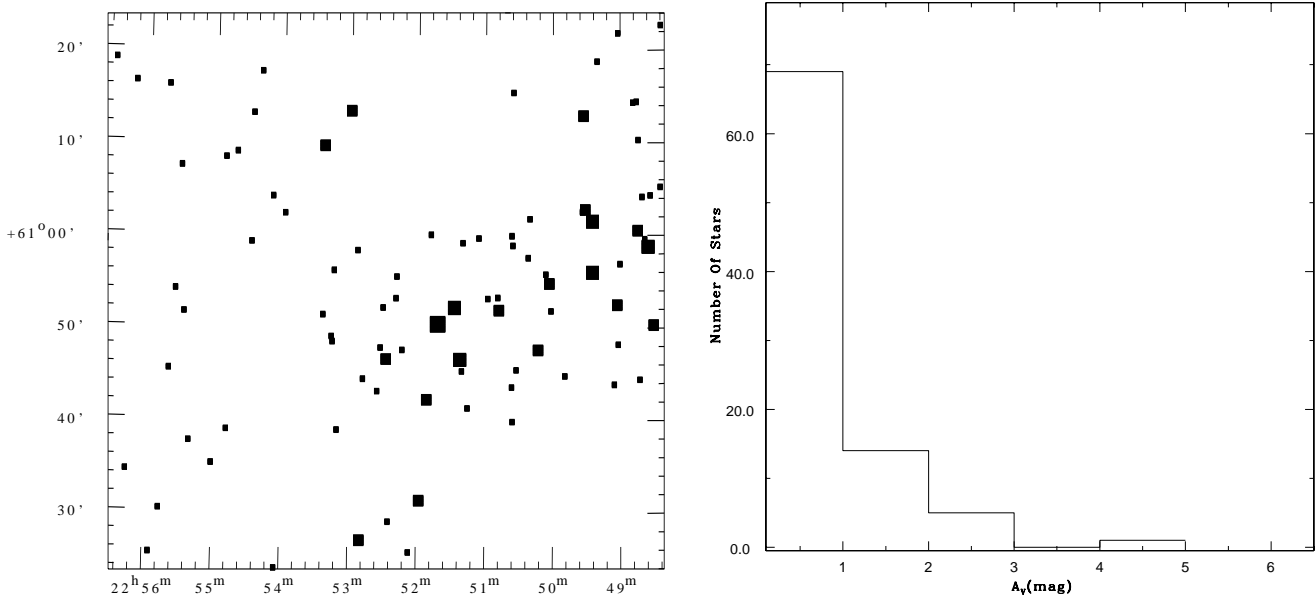


**Figure 13.** Distribution of the reddening. *left panel :* Spatial distribution of the reddening of the YSO candidates. Increasing sizes of filled boxes represent YSOs having $A_V$ with ranges $0-1$ mag, $1-2$ mag, $2-3$ mag and $4-5$ mag, respectively. X-axis and Y-axis denote RA$_{\rm J2000}$ and DEC$_{\rm J2000}$, respectively. *right panel :* Frequency distribution of the reddening for YSO candidates.

ner ($r \leq 1'$) and the outer ($1' \leq r \leq 3'.5$) region of the cluster, respectively, as well as for the whole cluster region ($r \leq 3'.5$) are given in Table 11 and plotted in Figure 16.

The slope of the MF of the main-sequence stars in the inner region of the cluster is estimated as $\Gamma = -0.19 \pm 0.15$, which is flatter than the Salpeter (1955) value, while for the stars in the outer region, $\Gamma = -1.52 \pm 0.18$, which is similar to the Salpeter (1955) value. The $\Gamma$ value for the stars is thus steeper in the outer region indicating a preferential distribution of relatively massive stars towards the cluster center indicating a segregation of stellar masses. The slope for the MF for the whole cluster is $\Gamma = -1.10 \pm 0.19$, which is similar to the Salpeter value in the mass range of $8.6 - 1.4 M_\odot$.

This value of the MF is similar to the value estimated by Beauchamp, Moffat & Drissen (1994) i.e. $\Gamma = -1.25 \pm 0.10$ estimated at age$\sim$14 Myr and distance $\sim 2.3$ kpc for the cluster region.

The slopes of the pre-main-sequence MF for the intermediate mass range $7 - 3 M_\odot$ in the cluster are derived as $\Gamma = +1.54 \pm 0.52$ for inner, $\Gamma = +1.64 \pm 1.52$ for outer, and $\Gamma = +1.68 \pm 0.84$ for whole cluster region. The value of the pre-main-sequence MF slope is significantly flatter than the Salpeter value.
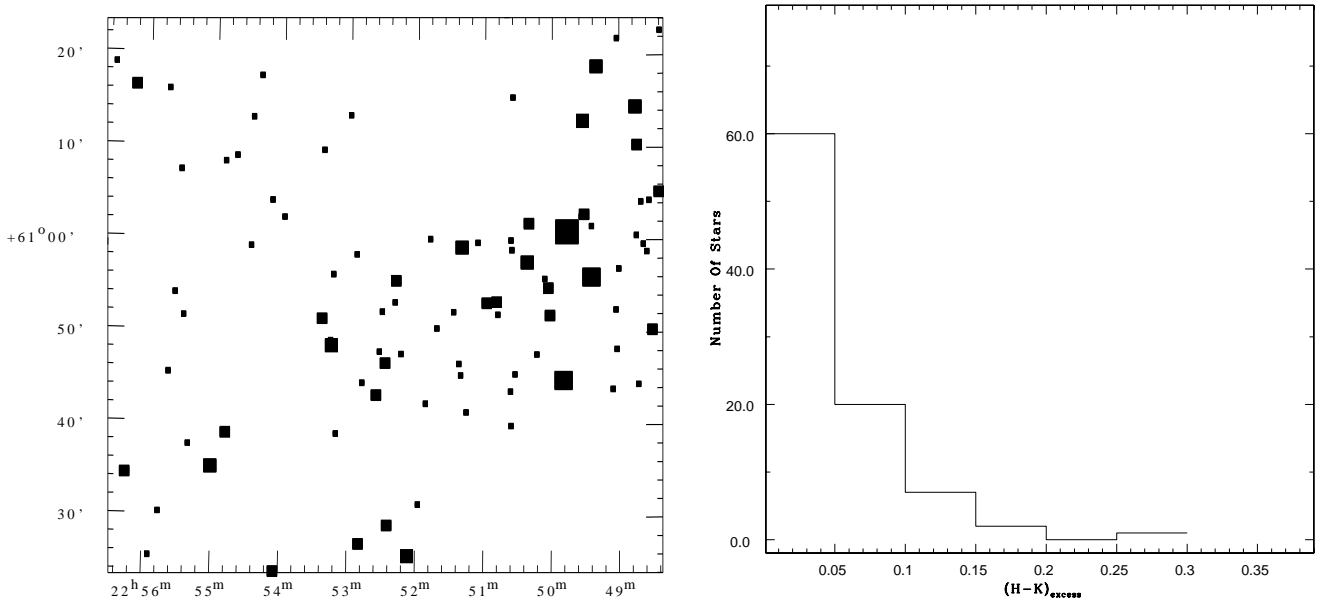
**Figure 14.** Age spread of YSOs. *left panel :* Spatial distribution of the $(H - K)_{\mathrm{excess}}$ of the YSO candidates. The increasing sizes of filled boxes represent the YSOs having $(H - K)_{\mathrm{excess}}$ in ranges $0 - 0.05$ mag, $0.05 - 0.10$ mag, $0.10 - 0.15$ mag, $0.15 - 0.20$ mag and $0.25 - 0.30$ mag, respectively. X-axis and Y-axis denote $\mathrm{RA_{J2000}}$ and $\mathrm{DEC_{J2000}}$, respectively. *right panel:* Frequency distribution of the $(H - K)_{\mathrm{excess}}$ for YSO candidates.

**Table 11.** The MF of the cluster NGC 7419. MS represent the MF for main-sequence population while PMS represents the MF for pre-main sequence population. The numbers of probable cluster members (N) have been obtained after subtracting the expected contribution of field stars in §3.2. $\log\phi$ represents log N(log m).

| Magnitude range ($V$ mag) | Mass Range ($M_\odot$) | Mean log ($M_\odot$) | Inner region N | Inner region $\log\phi$ | Outer region N | Outer region $\log\phi$ | Whole region N | Whole region $\log\phi$ |
|---|---|---|---|---|---|---|---|---|
| MS | | | | | | | | |
| 15.0 - 16.0 | 8.59 - 7.10 | 0.894 | 9 | 2.036 | 6 | 1.860 | 15 | 2.258 |
| 16.0 - 17.0 | 7.10 - 5.20 | 0.789 | 11 | 1.912 | 16 | 2.075 | 27 | 2.302 |
| 17.0 - 18.0 | 5.20 - 3.57 | 0.642 | 14 | 1.933 | 27 | 2.218 | 41 | 2.400 |
| 18.0 - 19.0 | 3.57 - 2.45 | 0.479 | 16 | 1.991 | 34 | 2.318 | 50 | 2.486 |
| 19.0 - 20.0 | 2.45 - 1.78 | 0.326 | 13 | 1.972 | 65 | 2.671 | 78 | 2.750 |
| 20.0 - 21.0 | 1.78 - 1.44 | 0.207 | 14 | 2.172 | 96 | 3.008 | 110 | 3.067 |
| PMS | | | | | | | | |
| | 7.00 - 6.00 | 0.544 | 4 | 1.505 | 7 | 1.748 | 11 | 1.945 |
| | 6.00 - 5.00 | 0.653 | 3 | 1.491 | 11 | 2.055 | 14 | 2.160 |
| | 5.00 - 4.00 | 0.740 | 5 | 1.800 | 4 | 1.703 | 9 | 2.056 |
| | 4.00 - 3.00 | 0.067 | 5 | 1.873 | 16 | 2.378 | 21 | 2.496 |

# 7   MASS SEGREGATION

There is evidence for mass segregation in a few Galactic as well as LMC star clusters, with the highest mass stars preferentially found towards the center of the cluster (see Sagar et al. 1988; Sagar & Richtler 1991; Sagar & Griffiths 1998; Pandey et al. 2001, 2005; Kumar, Sagar & Melnick 2008). It is a well accepted finding that stars in the clusters evolve rapidly towards a state of energy equipartition through stellar encounters i.e., mass segregation. However, observations of very young clusters (e.g., Sagar et al. 1988; Pandey, Mahra & Sagar 1992; Pandey et al. 2005; Hillenbrand 1997) suggest that the mass segregation may be the imprint of star formation itself.

We have subdivided the main-sequence sample (used for the main-sequence MF in §6) into two mass groups ($3.6 \leq M/M_\odot < 8.6$; $1.4 \leq M/M_\odot < 3.6$) to characterize the degree of mass segregation in NGC 7419. Figure 17 shows cumulative distribution of main-sequence stars as a function of radius in two different mass groups. Effect of mass segregation can be seen in this figure in the sense that more massive stars ($3.6 \leq M/M_\odot < 8.6$) tend to lie towards the cluster center. The Kolmogorov-Smirnov (KS) test confirms the statement that the cumulative distribution of massive stars in the cluster is different from that of relatively less massive stars at a confidence level of 99%. There is a strong evidence of mass segregation in the main-sequence stars within this cluster. We estimated the relaxation time
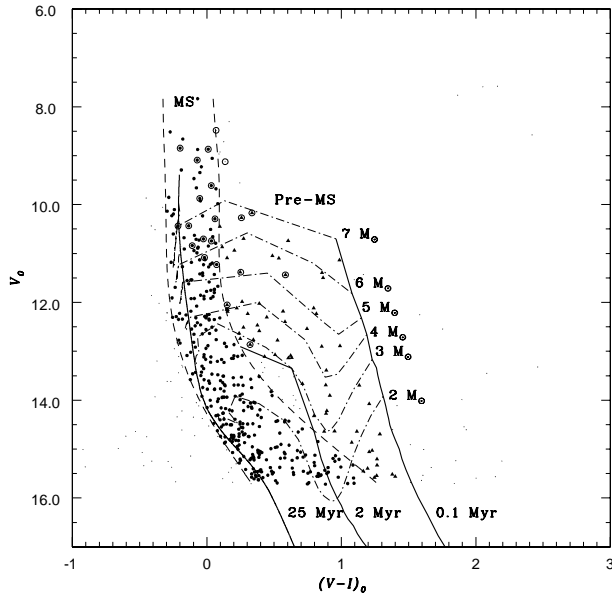
**Figure 15.** Extinction corrected CMD at mean $E(B-V)$=1.70 mag. Solid lines represent the theoretical isochrones for main-sequence at 25 Myr (GRD02) and pre-main-sequence at 2 Myr and 0.1 Myr (SES00). Solid dots within long-dash line show the stars selected for the estimation of main-sequence MF at 25 Myr i.e. first episode of star formation, while the triangles represent the stars used for pre-main-sequence MF. Herbig Ae/Be are shown by open circles. Herbig Ae/Be stars within main-sequence band (solid dots with open circles) have not been considered in estimation of main-sequence MF and included in the estimation of pre-main-sequence MF.

to decide whether the mass segregation discussed above is primordial or due to dynamical relaxation. To estimate the dynamical relaxation time $T_E$, we have used the relation

$$T_E = \frac{8.9 \times 10^5 N^{1/2} R_h^{3/2}}{\bar{m}^{1/2} log(0.4N)} \qquad (3)$$

where $N$ is the number of cluster stars, $R_h$ is the radius containing half of the cluster mass and $\bar{m}$ is the average mass of the cluster stars (Spitzer & Hart 1971). The total number of stars in the cluster region are estimated as 321 in the mass range ($1.4 \leq M/M_\odot < 8.6$). For the half mass radius, we have used half of the cluster extent i.e., 1.63 pc. Taking average mass of the cluster as 3.92 $M_\odot$, we have estimated the dynamical relaxation time $T_E$ for the cluster as 8.0 Myr, which is lower than the turn-off age of the cluster i.e., 19 – 25 Myr. Therefore, we can conclude that the cluster is dynamically relaxed.

## 8   X-RAY DATA ANALYSIS

We have used the archival X-ray data from the XMM-Newton observations of NGC 7419. The observations were proposed by Christian Motch to search for Be+white dwarfs binaries in NGC 7419. The observation details are given in Table 12. Our analysis is based on the CCD images from the European Photon Imaging Camera (EPIC). The details of the X-ray telescope and EPIC PN and MOS cameras are given by Jansen et al. (2001), Strüder et al. (2001) and Turner et al. (2001). Data reduction followed standard
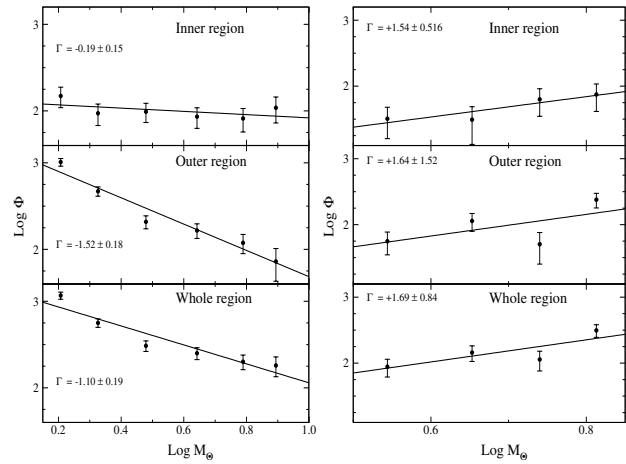


**Figure 16.** MF determination of MF in the various subregions of the cluster NGC 7419. *leftpanel* : for main-sequence and, for pre-main-sequence. *rightpanel* : Inner region represents the core region ($r \leq 1'$ ), Outer region represents the corona region ($1\rlap{.}'0 \leq r \leq 3\rlap{.}'5$ ) and Whole region represents the cluster region ($r \leq 3\rlap{.}'5$), as defined using radial density profile. The error bars represent $1/\sqrt{N}$ errors.
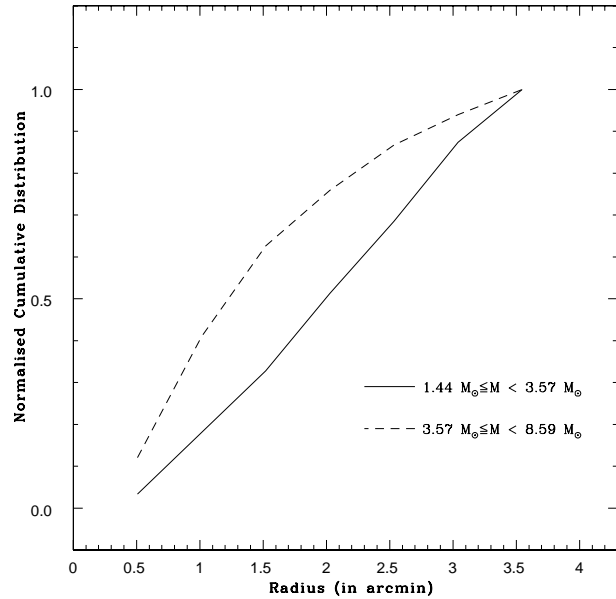


**Figure 17.** Cumulative radial distribution of main-sequence stars in mass intervals $1.44 \leq M/M_\odot < 3.57$ and $3.57 \leq M/M_\odot < 8.59$.

**Table 12.** XMM-Newton Observations of NGC 7419.

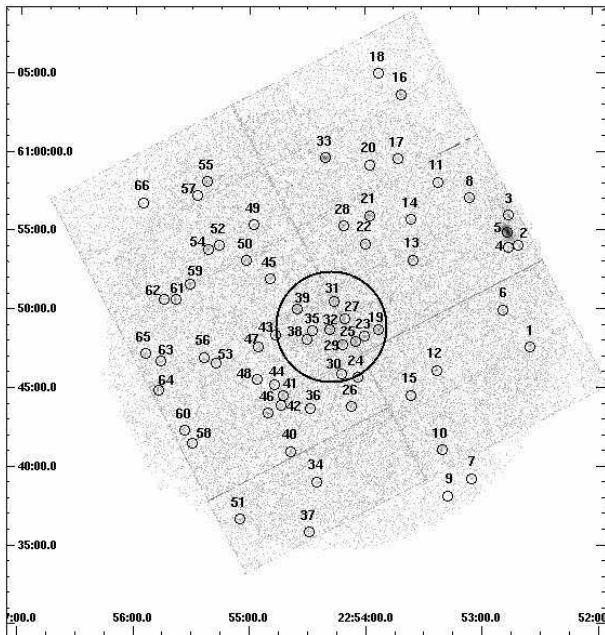| Parameter | NGC 7419 |
|---|---|
| Observation ID | 0201160501 |
| Start time (UT) | 02 Feb 2004 02:40:39 |
| Stop time (UT) | 02 Feb 2004 14:19:16 |
| Usable time(ks) | 39.62(MOS1),40.21(MOS2),35.35(PN) |
| EPIC mode | full frame |
| Optical filter | Medium |

**Figure 18.** The X-ray point sources in the mosaic image of MOS and PN detector in the energy band $0.3 - 7.5$ keV with their ID number as given in Table 13. X-axis and Y-axis denote RA$_{J2000}$ and DEC$_{J2000}$, respectively.

procedures using the XMM-Newton Science Analysis System software (SAS; version 7.0.0). Event files for MOS and PN are generated by using tasks *emchain* and *epchain*, respectively. Data from the three cameras were individually screened for high background episodes and the time intervals during which the total count rate (for single events of energy above 10 keV) in the instruments exceeded 0.35 and 1.0 counts s$^{-1}$ for the MOS and PN detectors, respectively, were excluded.

### 8.1    Source detection and identification

The source detection is based on the SAS point source detection algorithm *edetect_chain*. Three energy ranges were selected – a soft ($S_X$) band ($0.3 - 0.7$ keV), a medium ($M_X$) band ($0.7 - 1.2$ keV) and a hard ($H_X$) band ($1.2 - 7.5$ keV), and we built the corresponding images for the different instruments of the EPIC. Finally, source detection was performed on these images using *edetect_chain* task, which is a chain script of various sub tasks.

We inspected each source manually to reject false detections due to the instrumental artifacts, from the final list created by *emldetect* task. In this way, we found 66 sources with a combined maximum likelihood value greater than 10 in all three instruments. The details of all the genuine X-ray sources in the energy band $0.3 - 7.5$ keV are tabulated in Table 13 and shown in Figure 18.

We cross-correlated the X-ray source list with our optical $UBVRI$ photometric source list and NIR 2MASS All Sky data release data (Cutri et al. 2003) within the search radius $6''$. The position of the stars in optical CCD are converted into RA$_{J2000}$ and DEC$_{J2000}$ using the Guide Star Catalogue-II (GSC 2.2, 2001). There are 18 X-ray sources with optical counterparts and 31 with NIR counterparts found after

cross-correlation. Furthermore, none of the Herbig Ae/Be stars is having an X-ray counterpart. The unidentified X-ray sources i.e., without having any optical or NIR counterparts within XMM-Newton field of view ($30' \times 30'$), are 31 in number (47% of the total).

### 8.2    The detection limit

The analysis of detection limits in the XMM-Newton field of view is equally important to decide the X-ray emission level of undetected Herbig Ae/Be stars, as none of the Herbig Ae/Be stars is emitting X-rays. The faintest source detected above $2\sigma$ in the XMM-Newton field of view (FOV) has a count rate of $8.4 \times 10^{-4}$ counts s$^{-1}$ in the PN detector. The detection limit is not constant throughout the field of view because of the following three reasons: (a) a gap between the CCDs, and unoverlapped detector areas leading to a non-uniform effective detection area, (b) the decreasing exposure duration from the FOV center to its edges, causing a non-uniformity in the effective exposure times as well, and (c) the dense population of the stars near the center of the cluster affecting the detection limit non-uniformly. We have neglected the effects of the gap between CCDs, as an approximation, and investigated the effects of other parameters on the detection limit.

We analyzed the exposure map created by the *expmap* task for the PN detector in the energy band $0.3 - 7.5$ keV to derive the effect of exposure duration. It displays a smooth decrease in the counts from the center of the FOV to its edges by about a factor of three. If we are not considering the background effect, the signal-to-noise ratio is smaller by a factor of $\sqrt{3} \approx 1.7$ for the source at the edges of the FOV compare to the source at the center. Therefore, the detection limit in the edges of the FOV will be twice the detection limit at the center of the FOV due to the non-uniformity of exposure duration.

The variations in the detection limit due to the dense clustering at the center of FOV have been determined using the approach by Sana et al. (2006). We computed an equivalent PN count rate in the energy band $0.3 - 7.5$ keV due to the gap between CCDs. An empirical relation between count rates in the PN and MOS detectors was calculated and found to be approximately linear. For the sources which fall in the gaps between the PN CCDs, this relation is used to convert the MOS count rates into the PN count rates and these PN count rates are called pn-equivalent count rates. Figure 19, left panel, displays the source pn-equivalent count rates as a function of the distance from the center of the FOV i.e., the center of the cluster NGC 7419. We adjusted a four-degree polynomial by selecting the faintest sources to derive an empirical detection limit in terms of pn-equivalent count rates ($cr_{lim}$) as a function of distance ($d$) from the center of the FOV. This detection limit (in units of $10^{-3}$ counts s$^{-1}$) is shown by a solid line in Figure 19, left panel and described by the following relation:

$$cr_{lim}(d) = 2.246 - 0.999d + 0.267d^2 - 0.028d^3 + 0.001d^4 \quad (4)$$

where the distance $d$ is expressed in arcmin from the center of the FOV. Left panel of Figure 19 shows that the detection limit is higher in center of the FOV ($d < 3'.5$), which is the cluster region as decided in §3.1. It might be the effect of the extended X-ray emission from the cluster

**Table 13.** X-ray Sources detected using SAS task *edetect_chain*. Column 1 (XID), represents the identification number from X-ray source detection and display in Figure 18, Column 2 (Position), shows source position from X-ray source detection, Column 3 (Count Rates), represents the pn-equivalent count rates in energy band 0.3 – 7.5 keV, Column 4 (Hardness ratio), $HR1$ and $HR2$, defined in text, the sign of $\leq$ represents the hardness ratio calculated after replacing zero counts by upper limits in either of the energy band, Column 5 (Remarks), for PCM (the X-ray sources with membership probability using Hardness Ratio – the X-ray sources inside the dotted box in Figure 20) IR (the X-ray sources with NIR counterparts within 6″search radius using 2MASS data) , OPT (the X-ray sources with optical counterparts within 6″ search radius using our $UBVRI$ photometry.) , Cl (the X-ray sources within cluster region NGC 7419 – see §3.1)

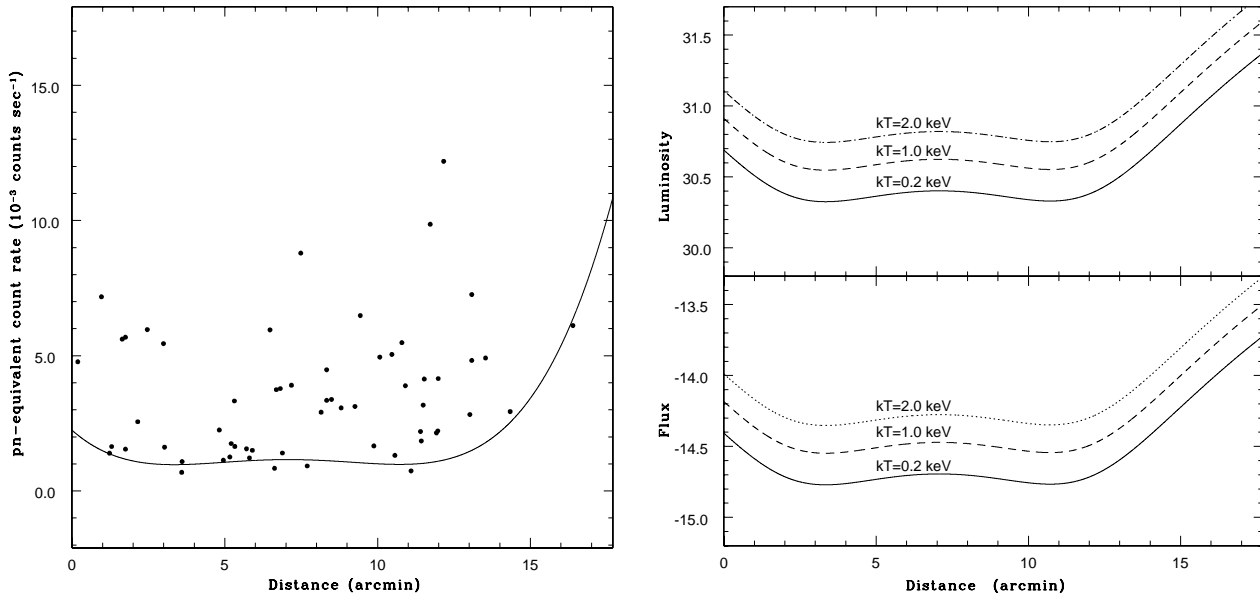| XID | $RA_{J2000}$ (h m s) | $DEC_{J2000}$ (° ′ ″) | Count Rates $10^{-3}$ counts s$^{-1}$ | Hardness ratio $HR1$ | $HR2$ | Remarks |
|---|---|---|---|---|---|---|
| 1 | 22 52 35 | 60 47 37 | 10.92± 1.50 | -0.40± 0.170 | 0.34 ± 0.21 | IR |
| 2 | 22 52 40 | 60 54 06 | 1.44± 0.58 | 0.25 ± 0.393 | ≤-0.20 | —— |
| 3 | 22 52 45 | 60 56 01 | 17.97± 1.58 | 0.16 ± 0.098 | -0.19 ± 0.11 | IR |
| 4 | 22 52 46 | 60 54 00 | 2.61± 0.74 | -0.01± 0.276 | -0.58 ± 0.48 | —— |
| 5 | 22 52 46 | 60 54 57 | 294.66± 5.33 | 0.47 ± 0.023 | -0.37 ± 0.02 | IR |
| 6 | 22 52 49 | 60 50 01 | 3.89± 0.73 | 0.82 ± 0.357 | 0.28 ± 0.19 | IR, PCM |
| 7 | 22 53 05 | 60 39 19 | 4.83± 2.06 | ≤-0.43 | ≤0.64 | —— |
| 8 | 22 53 06 | 60 57 08 | 4.15± 0.83 | 0.19 ± 0.512 | 0.77 ± 0.26 | —— |
| 9 | 22 53 17 | 60 38 13 | 2.82± 1.82 | 0.54 ± 0.565 | ≤-0.63 | IR |
| 10 | 22 53 21 | 60 41 09 | 5.05± 0.73 | 0.21 ± 0.167 | -0.10 ± 0.17 | IR |
| 11 | 22 53 22 | 60 58 08 | 2.20± 0.57 | 0.43 ± 0.255 | ≤-0.43 | —— |
| 12 | 22 53 23 | 60 46 12 | 3.91± 0.54 | 0.12 ± 0.145 | -0.34 ± 0.18 | IR |
| 13 | 22 53 35 | 60 53 12 | 3.75± 0.59 | 0.71 ± 0.683 | 0.83 ± 0.21 | PCM |
| 14 | 22 53 36 | 60 55 47 | 3.38± 0.61 | 0.69 ± 0.421 | 0.54 ± 0.21 | PCM |
| 15 | 22 53 37 | 60 44 37 | 0.84± 0.31 | ≤0.64 | 0.67 ± 0.44 | PCM |
| 16 | 22 53 41 | 61 03 43 | 18.95± 2.03 | 0.40 ± 0.118 | -0.50 ± 0.14 | IR |
| 17 | 22 53 42 | 60 59 38 | 3.18± 0.75 | 0.04 ± 0.233 | -0.10 ± 0.31 | IR |
| 18 | 22 53 52 | 61 05 04 | 6.12± 1.14 | ≤0.97 | 0.71 ± 0.23 | PCM |
| 19 | 22 53 53 | 60 48 48 | 5.45± 0.55 | 0.83 ± 0.331 | 0.70 ± 0.12 | IR, OPT, PCM, Cl |
| 20 | 22 53 57 | 60 59 14 | 1.32± 0.51 | 0.58 ± 0.406 | -0.41 ± 0.46 | IR |
| 21 | 22 53 57 | 60 56 02 | 8.79± 0.96 | ≤0.85 | 0.88 ± 0.15 | IR, PCM |
| 22 | 22 54 00 | 60 54 15 | 1.56± 0.41 | ≤0.70 | 0.63 ± 0.31 | PCM |
| 23 | 22 54 00 | 60 48 22 | 2.56± 0.43 | ≤0.70 | 0.75 ± 0.21 | OPT, PCM, Cl |
| 24 | 22 54 04 | 60 45 45 | 0.69± 0.24 | 0.08 ± 0.321 | 0.13 ± 0.19 | IR, OPT |
| 25 | 22 54 05 | 60 48 04 | 5.68± 0.71 | 0.07 ± 0.183 | 0.48 ± 0.16 | IR, OPT, Cl |
| 26 | 22 54 07 | 60 43 54 | 1.75± 0.37 | 0.28 ± 0.230 | -0.22 ± 0.26 | IR, OPT |
| 27 | 22 54 10 | 60 49 29 | 7.18± 1.17 | -0.56± 0.352 | 0.84 ± 0.25 | Cl |
| 28 | 22 54 11 | 60 55 23 | 5.96± 0.78 | 0.30 ± 0.137 | -0.51 ± 0.18 | IR |
| 29 | 22 54 12 | 60 47 51 | 1.64± 0.37 | ≤-0.48 | 0.75 ± 0.28 | IR, OPT, Cl |
| 30 | 22 54 12 | 60 45 59 | 1.62± 0.33 | 0.09 ± 0.20 | -0.98 ± 0.39 | IR, OPT, Cl |
| 31 | 22 54 16 | 60 50 36 | 5.61± 0.73 | -0.16± 0.17 | 0.41 ± 0.17 | IR, OPT, Cl |
| 32 | 22 54 18 | 60 48 48 | 4.78± 0.71 | ≤0.37 | 0.53 ± 0.17 | IR, OPT, Cl |
| 33 | 22 54 21 | 60 59 42 | 24.48± 1.52 | 0.02 ± 0.06 | -0.65 ± 0.10 | —— |
| 34 | 22 54 25 | 60 39 07 | 1.66± 0.40 | 0.49 ± 0.25 | ≤-0.25 | IR |
| 35 | 22 54 27 | 60 48 44 | 1.40± 0.38 | 0.60 ± 0.52 | 0.50 ± 0.31 | PCM, Cl |
| 36 | 22 54 29 | 60 43 49 | 1.64± 0.55 | -0.06± 0.29 | ≤-0.18 | IR, OPT |
| 37 | 22 54 29 | 60 35 57 | 7.26± 2.37 | ≤-0.24 | ≤0.84 | —— |
| 38 | 22 54 30 | 60 48 12 | 1.54± 0.36 | 0.85 ± 0.69 | 0.65 ± 0.28 | OPT, PCM, Cl |
| 39 | 22 54 35 | 60 50 05 | 5.96± 1.05 | 0.60 ± 0.20 | -0.43 ± 0.21 | OPT, Cl |
| 40 | 22 54 39 | 60 41 03 | 4.48± 0.59 | 0.32 ± 0.14 | -0.58 ± 0.19 | IR |
| 41 | 22 54 42 | 60 44 38 | 3.33± 0.84 | ≤-0.14 | ≤0.79 | IR, OPT |
| 42 | 22 54 44 | 60 44 01 | 1.50± 0.39 | ≤0.46 | ≤0.60 | —— |
| 43 | 22 54 46 | 60 48 27 | 1.09± 0.32 | 0.37 ± 0.91 | 0.80 ± 0.38 | —— |
| 44 | 22 54 47 | 60 45 18 | 1.25± 0.34 | ≤0.78 | ≤0.56 | PCM |
| 45 | 22 54 49 | 60 52 01 | 1.14± 0.35 | ≤0.78 | ≤0.53 | PCM |
| 46 | 22 54 50 | 60 43 29 | 3.78± 0.54 | 0.93 ± 0.83 | 0.87 ± 0.19 | OPT, PCM |
| 47 | 22 54 55 | 60 47 42 | 2.25± 0.42 | 0.31 ± 0.21 | -0.03 ± 0.22 | IR, OPT |
| 48 | 22 54 56 | 60 45 37 | 1.22± 0.36 | 0.43 ± 0.40 | 0.23 ± 0.32 | IR, OPT |
| 49 | 22 54 58 | 60 55 27 | 2.91± 0.56 | ≤0.74 | 0.88 ± 0.29 | PCM |
| 50 | 22 55 02 | 60 53 11 | 1.40± 0.48 | ≤0.86 | ≤0.60 | PCM |
| 51 | 22 55 05 | 60 36 45 | 4.92± 2.32 | ≤0.93 | ≤0.79 | PCM |
| 52 | 22 55 16 | 60 54 07 | 3.07± 0.60 | 0.97 ± 0.72 | 0.72 ± 0.24 | IR, OPT, PCM |
| 53 | 22 55 17 | 60 46 39 | 0.92± 0.37 | ≤0.70 | 0.82 ± 0.52 | IR, OPT, PCM |
| 54 | 22 55 22 | 60 53 52 | 3.12± 0.61 | ≤0.96 | 0.63 ± 0.23 | PCM |
| 55 | 22 55 22 | 60 58 10 | 12.19± 1.22 | 0.01 ± 0.11 | -0.30 ± 0.14 | IR |
| 56 | 22 55 24 | 60 47 02 | 3.35± 0.97 | -0.23± 0.64 | 0.76 ± 0.39 | —— |
| 57 | 22 55 27 | 60 57 18 | 2.14± 0.61 | 0.20± 0.27 | -0.70 ± 0.44 | —— |
| 58 | 22 55 30 | 60 41 35 | 4.14± 1.05 | -0.62± 0.41 | 0.74 ± 0.42 | —— |
| 59 | 22 55 31 | 60 51 39 | 6.48± 1.25 | -0.46± 0.45 | 0.84 ± 0.28 | —— |
| 60 | 22 55 34 | 60 42 23 | 1.85± 0.55 | ≤0.99 | ≤0.54 | PCM |
| 61 | 22 55 38 | 60 50 42 | 4.95± 0.77 | ≤0.87 | ≤0.79 | PCM |
| 62 | 22 55 44 | 60 50 43 | 5.48± 1.08 | -0.76± 0.44 | 0.91 ± 0.32 | —— |
| 63 | 22 55 46 | 60 46 48 | 7.41± 0.48 | ≤0.93 | ≤-0.12 | PCM |
| 64 | 22 55 47 | 60 44 58 | 9.86± 1.08 | 0.58 ± 0.13 | -0.42 ± 0.13 | IR |
| 65 | 22 55 54 | 60 47 14 | 2.22± 0.63 | 0.10 ± 1.50 | 0.94 ± 0.39 | —— |
| 66 | 22 55 56 | 60 56 50 | 2.94± 0.83 | -0.02± 0.30 | 0.14 ± 0.37 | IR |

**Figure 19.** The variation of X-ray detection limits within XMM-Newton field of view in energy band 0.3 — 7.5 keV. *leftpanel* : The distribution of the pn-equivalent count rates of the X-ray sources as a function of their distance from the center of the cluster NGC 7419. The solid line shows the adopted lower limit given in equation (4). (b)*rightpanel*: *Lower panel* : estimated detection limit expressed in terms of the observed flux (log(erg s$^{-1}$ cm$^{-2}$)), *Upper panel* : the detection limit, expressed in luminosity (log(erg s$^{-1}$)) using the distance of the cluster NGC 7419.

region, discovered in §8.5. The detection limit increases towards the CCD edges, as estimated by the exposure map. Using mission count rate simulator, WebPIMMS[7], we converted the pn-equivalent count rates into fluxes and luminosities. Assuming a hydrogen column density ($N_H$) of $9.9 \times 10^{21}$ cm$^{-2}$, at $E(B - V)$ =1.70 mag for the cluster NGC 7419, the Raymond-Smith single temperature optically thin thermal plasma models were used at temperatures (kT) of 0.2 keV, 1.0 keV and 2.0 keV. Results are displayed in Figure 19, right panel for different plasma temperatures. Luminosities are calculated for the distance of the cluster NGC 7419 i.e., 3.2 kpc. Within the cluster region ($d < 3.5$), the detection limit of flux varies from $1.66 \times 10^{-15}$ to $3.89 \times 10^{-15}$ erg cm$^{-2}$ s$^{-1}$ for soft X-ray sources at kT=0.2 keV, $3.02 \times 10^{-15}$ to $6.31 \times 10^{-15}$ erg cm$^{-2}$ s$^{-1}$ for X-ray sources at kT=1.0 keV, and $4.47 \times 10^{-15}$ to $10.0 \times 10^{-15}$ erg cm$^{-2}$ s$^{-1}$ for X-ray sources at kT=2.0 keV. We have estimated the detection limit of 21 Herbig Ae/Be stars, according to their positions in the cluster region using equation 4. As majority of Herbig Ae/Be stars have X-ray temperatures greater than 1.0 keV (Stelzer et al. 2006; Hamaguchi, Yamauchi & Koyama 2005), the detection limits for these stars are estimated as the median of the limiting X-ray luminosity (L$_X$) of Herbig Ae/Be stars i.e., $5.20 \times 10^{30}$ erg s$^{-1}$.

### 8.3  Probable Members Using Hardness Ratio

We have determined the X-ray hardness ratio $HR1$ and $HR2$ defined as

$$HR1 = \frac{(M_X - S_X)}{(M_X + S_X)} \tag{5}$$

$$HR2 = \frac{(H_X - M_X)}{(H_X + M_X)} \tag{6}$$

where $S_X$, $M_X$ and $H_X$ denote the soft band ($0.3 - 0.7$ keV), the medium band ($0.7 - 1.2$ keV) and the hard band ($1.2 - 7.5$ keV), respectively. For undetected sources, we used upper limits as a function of distance from the center of FOV to its edges in each the energy bands using the method mentioned in §8.2. In cases where no counts are observed in any one energy band, the $HR1$ or $HR2$ are either +1.0 (no soft counts) or -1.0 (no hard counts), we have replaced the zero counts value by the upper limits depending upon the source position in the CCD in that energy band. The hardness ratios $HR1$ and $HR2$ of the X-ray sources in the XMM-Newton FOV are displayed in Figure 20. X-ray sources are represented by solid dots, X-ray sources having optical counterparts, NIR counterparts and extended behavior are denoted by open circles, open squares and the symbol of star, respectively. X-ray sources with rightward arrows represent the upper limits in $HR1$, and downward arrows represent the upper limits in $HR2$. Solid lines represent hardness ratios derived from model spectra.

We have simulated the values of $HR1$ and $HR2$ using plasma model APEC (Atomic Plasma Emission Code) to relate these hardness ratios to the spectral properties of the sources and to decide the membership of X-ray sources in the cluster region. Using the EPIC-pn response matrices within XSPEC, we have generated model spectra for monothermal plasma (1T-APEC) and two-temperature plasma (2T-APEC : the coronal X-ray emission from active late-type stars is generally not monothermal and consistent with the 2T thermal plasma models, (see Favata et al. 2003; Tsujimoto et al. 2002; Stelzer et al. 2006)). We considered

---

[7] WebPIMMS is a NASA's HEASARC tool powered by PIMMS version 3.9. It is hosted at URL: http://heasarc.gsfc.nasa.gov/Tools/w3pimms.html
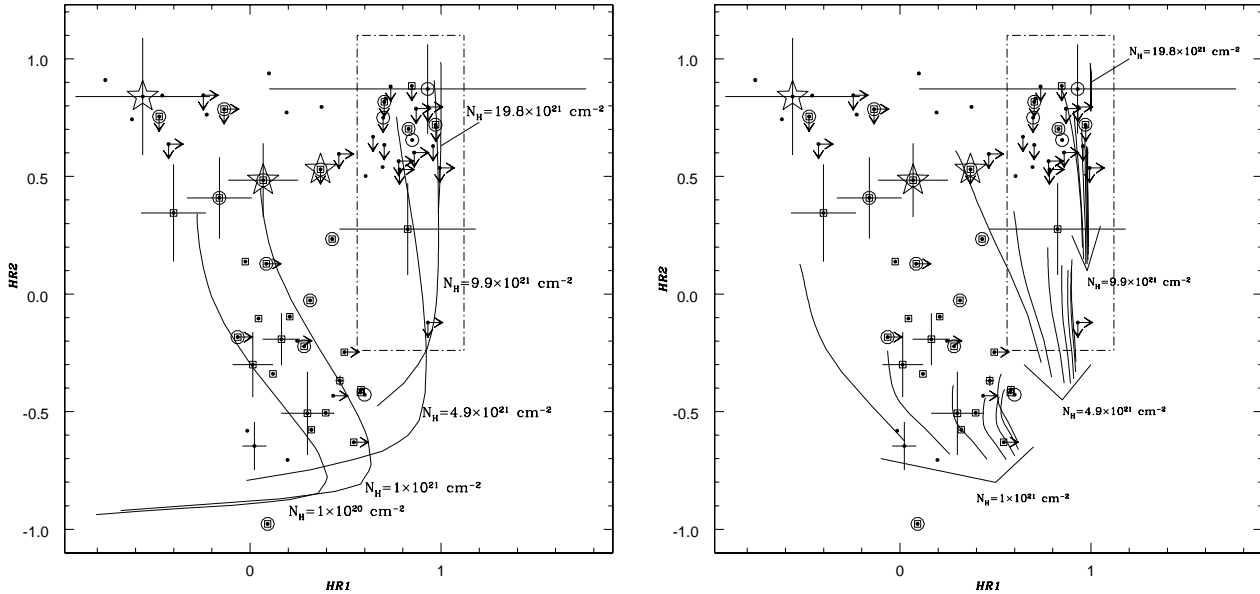
**Figure 20.** $HR1$ vs $HR2$ diagram for the X-ray sources denoted by solid dots. X-ray sources with optical counterparts, NIR counterparts and extended behavior are denoted by open circles, open squares and the symbol of star, respectively. X-ray sources with rightward arrow represent the upper limits in $HR1$, and downward arrow represent the upper limits in $HR2$. Solid lines represents $HR1$ vs $HR2$ curves obtained from APEC model and dotted box contains the X-ray probable members sharing the cluster environment. *left panel* For the single temperature 1T-APEC plasma model, we considered plasma temperatures of kT ranges from 0.2 to 8.0 keV, at different hydrogen column density $(N_H)= 1.0 \times 10^{20}$, $1.0 \times 10^{21}$, $4.9 \times 10^{21}$, $9.9 \times 10^{21}$ (for cluster region), $19.8 \times 10^{21}$ cm$^{-2}$. The temperature increases from bottom to top for each $N_H$ value. *right panel* The two temperature 2T-APEC plasma model with kT1 = 0.2, 0.3, 0.4, 0.5, 0.6, 0.7, 0.8 keV with the combination of kT2 ranges from 0.9 to 9.6 keV, at different hydrogen column density $(N_H)= 1.0 \times 10^{21}$, $4.9 \times 10^{21}$, $9.9 \times 10^{21}$ (for cluster region), $19.8 \times 10^{21}$ cm$^{-2}$. The temperature kT1 increases from left to right for each $N_H$ value with increasing kT2 from bottom to top.

plasma temperatures (kT) from 0.2 keV to 8.0 keV for 1T-APEC model, and kT1 from 0.2 to 0.8 keV with the combination of kT2 from 0.9 to 9.6 keV for 2T-APEC model at different hydrogen column density $(N_H)=1.0 \times 10^{20}$, $1.0 \times 10^{21}$, $4.9 \times 10^{21}$, $9.9 \times 10^{21}$ (for cluster region), $19.8 \times 10^{21}$ cm$^{-2}$.

The X-ray sources lying in between $1 \times 10^{20} < N_H < 1 \times 10^{21}$ cm$^{-2}$ are probably the foreground stars having either NIR counterparts or optical counterparts. As the value of mean $N_H$ for the cluster is estimated as $9.9 \times 10^{21}$ cm$^{-2}$ from the optical studies, X-ray stars located in between $4.9 \times 10^{21} < N_H < 19.6 \times 10^{21}$ cm$^{-2}$ belong to nearly the same cluster environment. In Figure 20, the X-ray sources situated inside the dotted box are considered as probable members belonging to the cluster. Most of the X-ray sources inside this box are having only upper limits in the soft bands and have hard spectra, which is a consequence of the absorption of the soft components of the energy by the large column densities. A few sources are fitted neither by 1T-APEC model nor 2T-APEC model and show a soft energy component as well as a hard energy component. Most of these sources are unidentified sources not having any NIR or optical counterparts. They may be the foreground stars, whose positions are uncertain in hardness ratio diagram because of the large uncertainty in the hardness ratios. But, for a few X-ray sources, the uncertainty in hardness ratios is not so large that their location can be explained within the temperature range of the models. They may be either the foreground stars having very high hard energy component greater than 9 keV or the 1T-APEC and 2T-APEC model are not enough to characterise them.
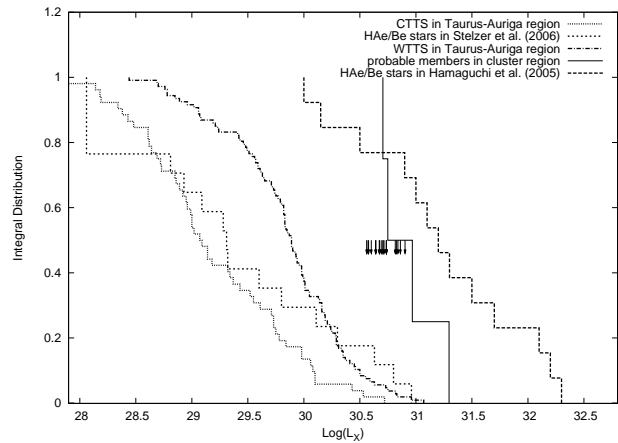


**Figure 21.** XLF for the probable members in the cluster region NGC 7419, weak-lined (WTTS) and classical T-Tauri stars (CTTS) in Taurus-Auriga region, and Herbig Ae/Be (HAe/Be) stars from Stelzer et al. (2006) and Hamaguchi, Yamauchi & Koyama (2005) using Kaplan-Meier estimator. The downward arrows represent 21 Herbig Ae/Be stars in the cluster NGC 7419.

## 8.4 X-ray Luminosity Function

X-ray luminosity function (XLF) is frequently employed to characterize a stellar population. We performed statistical analysis of XLF using Kaplan-Meier estimator of integral distribution functions. We have derived the median $L_X$ of weak-lined and classical T-Tauri stars in Taurus-
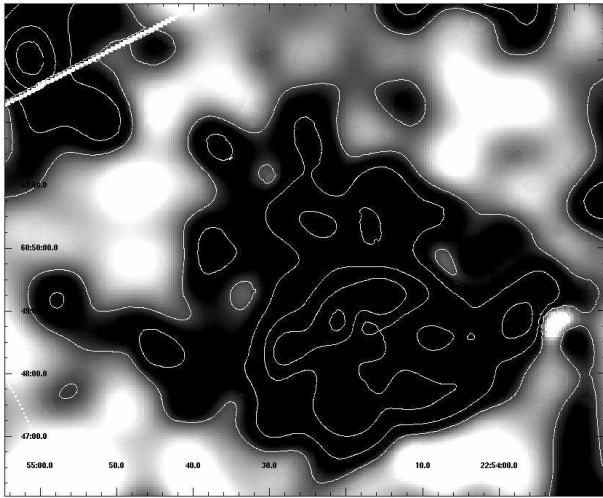
**Figure 22.** The X-ray extended emission from the cluster NGC 7419 in mosaic MOS detector in energy band the $1.2 - 7.5$ keV. X-axis and Y-axis denote RA$_{J2000}$ and DEC$_{J2000}$, respectively. The gray scale is logarithmic to highlight the diffuse component. The contours are plotted at 4.104 (above $3\sigma$ of the background), 4.644, 5.418, 6.192, 6.966 $10^{-3}$ counts s$^{-1}$ arcmin$^{-2}$.
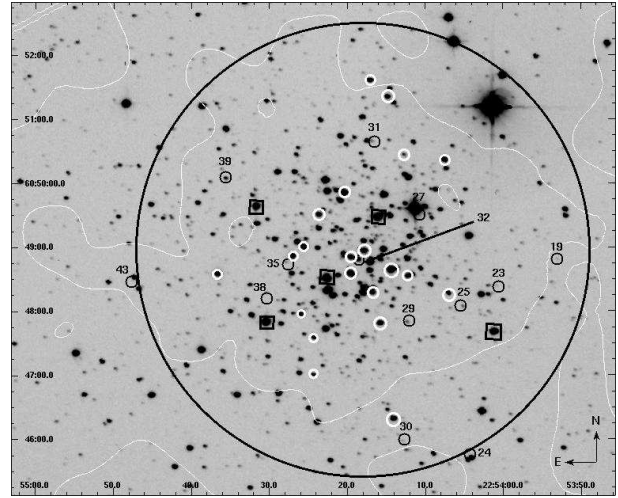


**Figure 23.** Overlay of X-ray point sources (black open circles) with ID from Table 13 and 21 Herbig Ae/Be stars (white open circles) in the cluster region NGC 7419. Large black circle represent the cluster region and black squares represent supergiants. X-axis and Y-axis denote RA$_{J2000}$ and DEC$_{J2000}$, respectively. The white contours represent the extended X-ray emission in energy band $1.2 - 7.5$ keV above the $3\sigma$ of the background count rate i.e. the outermost contour of the Figure 22.

Auriga region (age= $0.1 - 10$ Myrs) using the data from Stelzer & Neuhäuser (2001) and for Herbig Ae/Be stars, we have used the sample of Stelzer et al. (2006) and Hamaguchi, Yamauchi & Koyama (2005). The median L$_X$ of four probable members in the cluster is estimated as 30.75 erg s$^{-1}$. For weak-lined T-Tauri, classical T-Tauri, and Herbig Ae/Be stars in the sample of Stelzer et al. (2006) and Hamaguchi, Yamauchi & Koyama (2005), the median L$_X$ have been estimated as 29.88, 29.07, 29.29 and 31.15 erg s$^{-1}$, respectively. A comparison of the XLFs of T-Tauri stars and Herbig Ae/Be stars with the cluster members are shown in Figure 21.

The X-ray upper limits indicate that the Herbig Ae/Be stars in NGC 7419 are not systematically more active than T-Tauri in Taurus-Auriga region and Herbig Ae/Be stars in Stelzer et al. (2006). But the median value of XLF of Herbig Ae/Be stars in Hamaguchi, Yamauchi & Koyama (2005) is more than the upper limits in the cluster. Our exposure and resolution (see §8.5) are not enough to reach the median value of L$_X$ of T-Tauri stars, therefore, we can not conclude whether Herbig Ae/Be stars can have an XLF similar to either the T-Tauri stars or Herbig Ae/Be stars in Stelzer et al. (2006). A much deeper detection level is clearly needed in order to reach definitive conclusions concerning in the X-ray emission from Herbig Ae/Be stars. However, the more important conclusion to draw from this analysis is that the Herbig Ae/Be stars in NGC 7419 are not as active as in the sample of Hamaguchi, Yamauchi & Koyama (2005).

## 8.5 Extended X-ray Emission

The extended emission from the cluster region NGC 7419 has been studied using MOS images. PN data were not used since chip gaps, bad columns, and the the out-of-time event correction would have complicated the analysis. We have created the MOS images and associated exposure maps in three bands: soft band ($0.3 - 0.7$ keV), medium band ($0.7$

$- 1.2$ keV) and hard band ($1.2 - 7.5$ keV). We have chosen adaptive smoothstyle with signal-to-noise ratio 10 in the task *asmooth*, for getting the faint emission from the cluster region. The resulting mosaic image with point sources are weighted, masked and exposure-corrected following the procedure described in the documentation for the SAS task *asmooth* [8]. The point sources are removed from the image using cheesemask but the background is not subtracted from it.

The signature of extended emission is not present in the soft band ($0.3 - 0.7$ keV) and medium band ($0.7 - 1.2$ keV) images of the MOS, because of the the absorption of the soft X-ray component due to the large hydrogen column density ($N_H$). All the probable point sources have hard spectra, therefore, it is very likely that the extended emission is due to unresolved hard X-ray sources in the cluster. The X-ray contour map of the diffuse X-ray emission in energy band $1.2 - 7.5$ keV is shown in Figure 22. The entire cluster region is covered by the central CCD of the MOS, therefore, we have chosen background regions of 22745 pixels beyond the diffuse emission but within the central CCD. The contours are plotted above the $3\sigma$ of the mean background count rates. The extended X-ray emission from the cluster region contains 0.084 counts s$^{-1}$ in 14611 pixels and corresponds to $5.76\times10^{-6}$ counts s$^{-1}$ pixel$^{-1}$. The pixel size is set at $2'' \times 2''$. Therefore, the total extended emission has a size of 16.23 arcmin$^2$. We have estimated the count rate from the extended emission as $1.38\times10^{-3}$ counts s$^{-1}$ arcmin$^{-2}$, after subtracting the mean background count rate. Using WebPIMMS ver3.9a, this count rate is converted into flux after considering Raymond-Smith thermal plasma model at 1 keV and estimated as $1.47 \times 10^{-14}$ erg s$^{-1}$ cm$^{-2}$ arcmin$^{-2}$, which corresponds to

---

[8]  http://xmm.gsfc.nasa.gov/docs/xmm/sas/help/asmooth/index.html

the luminosity $L_X \approx 1.8 \times 10^{31}$ erg s$^{-1}$ arcmin$^{-2}$ in the energy band $1.2 - 7.5$ keV. We have chosen the beamwidth as 50 pixel i.e., $5\sigma$ (smoothing beam width). We have estimated 18 beam elements in per arcmin$^2$ region and estimated $L_X$ of unresolved sources as $1.0 \times 10^{30}$ erg s$^{-1}$. Therefore, we are expecting $\sim 288$ unresolved X-ray sources in the total diffuse component.

The $L_X$ of unresolved X-ray sources is comparable with the $L_X$ of T-Tauri stars i.e., $28 < \log L_X < 32$ in energy band 0.5 to 8.0 keV, with a peak around $\log L_X \sim 29$, (Feigelson et al. 2005). It can be explained by the presence of $\sim 288$ T-Tauri stars in the cluster, which are not resolved by XMM-Newton observatory. Higher resolution (sub arcsec) data are urgently required to explore this issue.

## 8.6 X-Ray emission and Herbig Ae/Be stars

We have examined a sample of 21 Herbig Ae/Be in this cluster using 2MASS data, H$\alpha$ photometry and the spectroscopic studies reported by Subramaniam et al. (2006). However, none of Herbig Ae/Be stars has an X-ray counterpart. In Figure 23, the distribution of the X-ray point sources which are having optical counterparts, supergiants (5 in number) and the Herbig Ae/Be stars within the cluster are shown by black open circles (with ID from Table 13), black open squares and white open circles, respectively.

The detection limit analysis §8.2 and the XLF (Figure 21) indicate that the $L_X$ observed from the low mass pre-main-sequence stars is less than upper limits of the detection (see, Stelzer & Neuhäuser 2001) i.e., $28 < \log L_X < 32$ in energy band 0.5 to 8.0 keV, with a peak around $\log L_X \sim 29$ erg s$^{-1}$, (Feigelson et al. 2005). Therefore, if a Herbig star is having a T-Tauri star as a binary companion, then we cannot detect the X-ray emission from it. Therefore, the generation of X-ray emission from Herbig Ae/Be stars (see, Zinnecker & Preibisch 1994; Damiani et al. 1994; Stelzer et al. 2006) might be the result of a T-Tauri binary companion which is not detectable in our study and we can not rule out the companion hypothesis for the generation of X-ray emission from Herbig Ae/Be stars. It might happen that the Herbig Ae/Be star itself is emitting X-rays but the level of the X-ray emission is less than the detection limit. A similar kind of process as in T-Tauri stars could then take place in the Herbig Ae/Be stars for the generation of X-rays.

## 9 SUMMARY AND CONCLUSIONS

A deep optical $UBVRI$ and narrow band H$\alpha$ observations along with multi-wavelength archival data from the surveys such as 2MASS, MSX, IRAS and XMM-Newton are used to understand the global scenario of star formation and the basic parameters of the cluster NGC 7419. XMM-Newton archival data have also been used to study the X-ray emission mechanism from the cluster.

The radius of the cluster NGC 7419 has been found to be $4'.0 \pm 0'.5$ using radial density profile. The reddening law in the direction of the cluster is found to be normal at longer wavelengths but anomalous at shorter wavelengths. Reddening, $E(B - V)$, is found to be varying between 1.5 to 1.9 mag with a mean value $\sim 1.7 \pm 0.2$ mag. The turn-off age and the distance of the cluster are estimated to be

$22.5 \pm 2.5$ Myr and $3230^{+330}_{-430}$, respectively. The MF for the main-sequence stars in the cluster is estimated as having $\Gamma = -1.10 \pm 0.19$ in the mass range $8.6 M_\odot < M \leq 1.4 M_\odot$, which is a similar to the Salpeter (1955) value. Effect of mass segregation is found in the main-sequence stars which may be the result of dynamical evolution.

Using the NIR color-color diagram and narrow band H$\alpha$ observations, we have identified 21 Herbig Ae/Be in the cluster region with the masses lying between 3 to $7 M_\odot$. The ages of these Herbig Ae/Be stars are found to be in the range of $\sim 0.3$ to 2.0 Myr. The significant difference between turn-off age and turn-on age of the cluster represents a second episode of star formation in the cluster. We have found 90 YSOs having masses in the range from 0.1 to $2.0 M_\odot$ with the help of NIR color-color diagram around the cluster. The presence of such a large number of NIR excess sources (T-Tauri stars) shows a recent star formation episode in the surroundings of the cluster region. Using extinction, dust and $^{12}$CO maps, we found that these YSOs are probably associated with a foreground star forming region Sh-154 and not related with the cluster region. We found no obvious trend in spatial distribution of YSOs with $A_V$ and $(H - K)_{\text{excess}}$. The dispersion in $A_V$ and $(H - K)_{\text{excess}}$ is also very low which indicates that a majority of the YSOs are born at the same time in the same environment. Therefore, it is possible that primordial fragmentation of the cloud may be responsible for the formation of the low mass stars within this cloud.

We have detected 66 X-ray sources in the observed field by XMM-Newton observatory using archival X-ray data. Out of these sources, 23 are knowm to be the probable members of the cluster based on analysis of their X-ray colors. Fifteen X-ray sources are without any optical or NIR counterparts. These may be the young embedded sources which need to be investigated further. We have derived the detection limits of X-ray observations based on the position of the X-ray source in the field of view and on its energy spectrum. Thus, the median value for the detection limit for the 21 Hebig Ae/Be stars in the field is $L_X \sim 5.2 \times 10^{30}$ erg s$^{-1}$. We have compared the XLF for the cluster members with the T-Tauri stars and Herbig Ae/Be stars. Because of insufficient exposure and resolution, the sensitivity was not enough to reach the level of the median X-ray luminosity observed in T-Tauri stars in Taurus-Auriga region and Herbig Ae/Be stars in Stelzer et al. (2006). Therefore a conclusive comparison of X-ray properties of the stars cannot be made. However, the comparison indicates that Herbig Ae/Be stars in NGC 7419 tend to be less X-ray luminous than in the sample of Hamaguchi, Yamauchi & Koyama (2005), which shows that X-ray activity level of the Herbig Ae/Be stars is not more than in the T-Tauri stars. Therefore, we can support the binary T-Tauri companion hypothesis for the generation of X-rays in Herbig Ae/Be stars. It is also possible that a Herbig Ae/Be star is itself emitting X-rays but the level of the X-ray emission is similar to that of the T-Tauri stars. The cluster region shows an extended X-ray emission with a total luminosity estimated to be $L_X \approx 1.8 \times 10^{31}$ erg s$^{-1}$ arcmin$^{-2}$. This diffuse emission might be the result of X-ray emission from T-Tauri type stars which could not be resolved by XMM-Newton observations. It requires $\sim 288$ T-Tauri stars each having $L_X \sim 1.0 \times 10^{30}$ erg s$^{-1}$, if it originates from such stars. High resolution deep observations such as from

CHANDRA are required for a detailed analysis of this cluster region.

## REFERENCES

Avedisova V. S., 2002, Astron. Reports, 46, 193

Beauchamp A., Moffat A. F. J., Drissen L., 1994, ApJS, 93, 187

Baume G., Vázqez R., Carraro G., 2004, MNRAS, 355, 475

Barbon R., Hassan S. M., 1996, A&AS, 115, 325

Bertout C., Basri G., Bouvier J., 1988, ApJ, 330, 350

Bessell M. S., 1979, PASP, 91, 589

Bessell M. S., Brett J. M., 1988, PASP, 100, 1134

Bhatt B. C., Pandey A. K., Mohan, V. Mahara H. S., Paliwal, D. C., 1993, Bull. Astron. Soc. India, 21, 33

Blanco V., Nassau J. J., Stock J., Wehlau W., 1955, ApJ, 121, 637

Blitz L., Fich M., Stark A. A., 1982, ApJS, 49, 183

Caldwell A. R. John, Cousins A. W. J., Ahlers C. C., Wamelen P. van, Maritz E. J., 1993, SssAAO Circ. 15

Cardelli J. A., Clayton G. C., Mathis J. S., 1989, ApJ, 345, 245

Caron G., Moffat A., St-Louis N., Wade G. A., 2003, AJ, 126, 1415

Cutri R. M., Skrutskie M. F., van Dyk S., Beichman C. A., Carpenter J. M., Chester T., Cambresy L., Evans T. et al., 2003, The IRSA 2MASS All-Sky Point Source Catalog, NASA/IPAC Infrared Science Archive http://irsa.ipac.caltech.edu/applications/Gator/

Damiani F., Micela G., Sciortino S., Harnden F. R. Jr., 1994, ApJ, 436, 807

Dobashi K., Uehara H., Kandori R., Sakurai T., Kaiden M., Umemoto T., Sato F., 2005, PASP, 57, 1

Dias W. S., Alessi B. S., Moitinho, A., Lépine J. R. D., 2002, A&A, 389, 871

Dougherty S. M., Waters L. B. F. M., Burk G., Cote J., Cramer N., van Kerkwijk M. H., Taylor A. R., 1994, A&A, 290, 609

Favata F., Giardino G., Sciortino S., Damiani F., 2003, A&A, 403, 187

Feigelson E. D., Getman K., Townsley L., Garmire G., Preibisch T., Grosso N., Montmerle T., Muench A., McCaughrean M., 2005, ApJS, 160, 379

Fitzgerald M. P., 1970, A&A, 4, 234

Girardi L., Bertelli G., Bressan A., Chiosi C., Groenewegen M. A. T., Marigo P., Salasnich B., Weiss A., 2002, A&A, 391, 195

Hamaguchi K., Yamauchi S., Koyama K., 2005, ApJ, 618, 360

Hernandez J., Calvet N., Hartmann L., Briceno C., Sicilia-Aguilar A., Berlind P., 2005, AJ, 129, 856

Hillenbrand L. A., Strom S. E., Vrba F. J., Keene J., 1992, ApJ, 397, 613

Hillenbrand L. A., 1997, AJ, 113, 1733

Huang F., Chen W. P., Hsiao W. S., 2006, JTAM, 4, 27

Jansen F., Lumb D., Altieri B., Clavel J., Ehle M., Erd C., Gabriel C., Guainazzi M. et al., 2001, A&A, 365, 1

Jeffries R. D., Oliveira J. M., Naylor, T., Mayne N. J., Littlefair S. P., 2007, MNRAS, 376, 580

Johnson H. L., Morgan W. W., 1953, ApJ, 117, 313

Johnson H. L., 1968, in Middlehurst B. M., Aller, L.H., eds, Nebulae and Interstellar Matter. Univ. Chicago, 191

Joshi Y. C., 2005, MNRAS, 362, 1259

Kaluzny J., Udalski A., 1992, Acta Astron., 42, 29

Kerton C. R., Brunt C. M., 2003, A&A, 399, 1083

Khalil A., Joncas G., Nekka F., 2004, ApJ, 601, 352

King, I., 1962, AJ, 67, 471

Koornneef J., 1983, A&A, 128, 84

Kroupa P., 2002, Science, 295, 82

Kukarkin B. V., Efremov Yu. N., Frolov M. S., Medvedeva G. I., Kholopov P. N., Kurochkin N. E., Kukarkina N. P., Perova N. B. et al., IBVS, 1968, 311, 1

Kumar Brijesh, Sagar Ram, Sanwal B. B., Bessell M. S., MNRAS, 353, 991

Kumar B., Sagar R., Melnick J., 2008, MNRAS, 386, 1380

Landolt A. U., 1992, AJ, 104, 340

Matsuyanagi I., Itoh Y., Sugitani K., Oasa Y., Mukai T., Tamura M., 2006, PASJ, 58, 29

Mayne N. J., Naylor T., Littlefair S. P., Saunders Eric S., Jeffries R. D., 2007, MNRAS, 375, 1220

Medhi, B. J., Maheswar G., Pandey J. C., Kumar T. S., Sagar R., 2008, MNRAS, 388, 105

Meyer M., Calvet N., Hillenbrand L. A., 1997, AJ, 114, 288

Moffat A. F. J., Vogt N., 1973, A&A, 23, 317

Naylor T., Jeffries R. D, 2006, MNRAS, 373, 1251

Nilakshi, Sagar R., 2002, A&A, 381, 65

Oasa Y., Tamura M., Nakajima Y., Itoh Y., Maihara T., Iwamuro F., Motohara K., Hayashi S. S. et al., 2006, AJ, 131

Pandey A. K., Mahra H. S., Sagar R., 1992, Bull. Astron. Soc. India, 20, 287

Pandey A. K., Durgapal A. K., Bhatt B. C., Mohan V., Mahra H. S., 1997, A&A, 122, 111

Pandey A. K., Nilakshi, Ougra K., Sagar R., Tarusawa K., 2001, A&A, 374, 504

Pandey A. K., Upadhyay K., Nakada Y. , Ogura K., 2003, A&A, 397, 191

Pandey A. K., Upadhyay K., Ougra K., Sagar R., Mohan V., Mito H., Bhatt H. C., Bhatt B. C., 2005, MNRAS, 358, 1290

Phelps R. L., Janes K. A., Montgomery K. A., 1994, AJ, 107, 1079

Pigulski A., Kopacki G., 2000, A&A, 146, 465

Press, W. H., Teukolsky, S. A., Vetterling, W. T., et al. 1992, Numerical recipes in FORTRAN. The art of scientific computing.

Price S. D., Egan M. P., Carey S. J., Mizuno D. R., Kuchar T. A., 2001, AJ, 121, 2819

Sagar Ram, 1987 MNRAS, 228, 483

Sagar R., Miakutin V. I., Piskunov, A. E., Dluzhnevskaia O. B., 1988, MNRAS, 234, 831

Sagar R., Richtler T., 1991, A&A, 250, 324.

Sagar R., Griffiths W. K., 1998, MNRAS, 299, 777

Salpeter E. E., 1955, ApJ, 121, 161.

Sana H., Gosset E., Rauw G., Sung H., Vreux J.-M., 2006, A&A, 454, 1063

Sandhu T. S., Pandey A. K., Sagar R, 2003, A&A, 408, 515

Schmidt - Kaler Th., 1982, In: Landolt/Bornstein, Numerical Data and Functional Relationship in Science and Technology, New series, Group VI, Vol. 2b, Scaifers K. & Voigt H. H. (eds.) Springer - Verlog, Berlin, p. 14

Siess L., Dufour E., Forestini M., 2000, A&A, 358, 593

Spitzer L. Jr., Hart M. H., 1971, ApJ, 164, 399

Stetson P. B., 1987, PASP, 99, 191

Stetson P. B., 1992, in ASP Conf. Ser. Vol. 25, Astronomical Data Analysis Software and Systems I. Astron. Soc. Pac., ed. Worrall D. M., & Biemesderfer C., Barnes J., San Francisco, 297

Stelzer B., Neuhäuser R., 2001, A&A, 377, 538

Stelzer B., Huélamo N., Micela G., Hubrig S., 2006, A&A, 452, 1001

Stephenson C. B., 1984, PW&SO, 3, 1

Strüder L., Briel U., Dennerl K., Hartmann R., Kendziorra E., Meidinger N., Pfeffermann E., Reppin C., 2001, A&A, 365, 18

Subramaniam A., Mathew B., Bhatt B. C., Ramya S., 2006, MNRAS, 370, 743

Tsujimoto M., Koyama K., Tsuboi Y., Goto M., Kobayashi N., 2002, ApJ, 556, 574

Turner M. J. L., Abbey A., Arnaud M., Balasini M., Barbera M., Belsole E., Bennie P. J., Bernard J. P. et al., 2001, A&A, 365, 27

Ungerechts H., Umbanhowar P., Thaddeus P., 2000, ApJ, 537, 221

van de Hulst H. C., Mullar C. A., Oort J., 1954, BAN, 12, 117

Wegner W., 1994, MNRAS, 270, 229

Whittet D. C. B., van Breda I. G., 1980, MNRAS, 192, 467

Zinnecker H., Preibisch T., 1994, A&A, 292, 152